



Mechanical-metallurgical-corrosion behavior of Cr-Si-S-C ferritic/ferromagnetic stainless steel, known as AISI 430F, before and after isothermal recrystallization annealing

Shahab Bazri¹ · Carlo Mapelli¹ · Silvia Barella¹ · Andrea Gruttadauria¹ · Davide Mombelli¹ · Renato Nempfardi² · Roberto Bedini² · Giorgio Zucchelli²

Received: 11 May 2023 / Accepted: 8 January 2024
© The Author(s) 2024

Abstract

The research investigates the mechanical and corrosion behavior of Cr-Si-S-C ferritic stainless steel (FSS), known as EN1.4105, which is equivalent to AISI430F. The static isothermal recrystallization annealing is applied to the cold-drawn (CD) materials with two different reduction rates (RRs) of 20 and 35%, under various conditions of soaking temperature and incubation time, which provide 42 unique specimens. The microstructures of CD and annealed materials are characterized by using the electron backscatter diffraction method. X-Ray diffraction analysis alongside scanning electron microscopy linked with energy-dispersive X-ray spectroscopy are also employed to scrutinize the precipitation of any secondary phases, morphologies, and the related chemical compositions. Two different corrosive chlorinated and acidic electrolyte solutions are used for the potentiostatic-based corrosion tests to investigate the passivation kinetics. The results show that the higher RR, which provides faster recrystallization, results in a higher scale of non-hardenable materials. In addition, the effects of RR and annealing conditions are found to have an impact on the corrosion resistance. Moreover, the material exhibits varied behavior in terms of both passivation layer formation as the immersion in the sulfuric acid electrolyte solution (SAES) and active electrochemical behavior immersing in sodium chloride electrolyte solution (SCES). However, this material shows lower corrosion current density and higher corrosion potential in the SCES compared to the SAES medium. The comprehensive findings underscore the intricate relationship between reduction rates, annealing conditions, microstructural evolution, and corrosion behavior in this FSS. The observed trends provide valuable insights for optimizing material performance and corrosion resistance in practical applications.

Keywords Ferritic stainless steel · Recrystallization annealing · Reduction rate · Microstructures · Mechanical-metallurgical-corrosion properties

Abbreviations

0.2OYS 0.2% Offset yield strength
AGS Average grain size

AIT Annealing incubation time
AST Annealing soaking temperature
CD Cold-drawn
DD Dislocation density
DL-EPR Double loop electrochemical potentiostatic repassivation
EBSD Electron backscatter diffraction
EDS Energy-dispersive X-ray spectroscopy
EHT Electron high tension
EIS Electrochemical impedance spectroscopy
FSS Ferritic stainless steel
GAM Grain average misorientation
GB Grain boundary
GOS Grain orientation spread
HAGB High-angle grain boundaries
IPF Inverse pole figure

Highlights

- Mechanical and corrosion behavior of cold-drawn and heat-treated Cr-Si-S-C FSS was investigated.
- A higher reduction rate led to faster recrystallization and formation of more equiaxed, finer, and smaller grains.
- Annealing of EN1.4105 FSS with a higher reduction rate resulted in improved targeted non-hardenable behavior.
- This grade also exhibited higher corrosion resistance at a lower reduction rate in both chlorinated and acidic environments.

Carlo Mapelli, Silvia Barella, Andrea Gruttadauria, Davide Mombelli, Renato Nempfardi, Roberto Bedini and Giorgio Zucchelli contributed equally.

Extended author information available on the last page of the article

KAM	Kernel average misorientation
LAGB	Low-angle grain boundaries
LM	Local misorientation
OCP	Open circuit potential
RD	Rolling direction
RF	Recrystallization fraction
RR	Reduction rate
SAES	Sulfuric acid electrolyte solution
SCES	Sodium chloride electrolyte solution
SEM	Scanning electron microscope
SFSS	Super ferritic stainless steel
SS	Stainless steel
TRAM	Temperature ratio between the annealing and melting point temperatures
UTS	The ultimate tensile strength
XRD	X-ray diffraction

Symbols

E_b	Breakdown potential
i_{cr}	Critical current density
E_{corr}	Corrosion potential
E_{oe}	Oxygen evolution potential
E_{pa}	Passive potential
E_{pit}	Pitting corrosion
E_{pp}	Primary passivation potential
E_{sp}	Secondary passivation potential
$R_{p0.2\%}$	0.2% Tensile strength
R_m	The ultimate tensile strength
TE	The total elongation

1 Introduction

Ferrous alloys such as ferritic stainless steel (FSS) are widely recognized for their noteworthy mechanical properties, including strength and ductility. However, for further enhancing their resistance to any type of corrosion such as electrochemical corrosion, mechanically induced wear corrosion, tribocorrosion et cetera, they are alloyed with complementary elements. In a broader outlook, stainless steels (SS) come in various grades that exhibit excellent corrosion resistance even in highly aggressive environments, namely, those containing acidic, chloride, and bromide substances, as demonstrated by Cao et al. [1]. Several factors contribute to this privilege, containing the presence of chromium, molybdenum, and/or nitrogen in the elemental compositions, as reported by Barella et al. [2]. As noted by Zhang et al. [3], and on further examination, it becomes evident that FSS with almost high levels of chromium and molybdenum are extensively employed in diverse industrial applications [4] although Lu et al.

[5] have hinted that the highest content of chromium belongs to super FSS which would be another class of materials. The widespread use of FSS in various environments can be attributed to their relatively good corrosion resistance alongside other properties like mechanical behavior and magnetic properties. For instance, in the automotive industry, achieving first-rate corrosion resistance is crucial, and Cai et al. [6] discussed the successful application of Fe-19Cr-2Mo-Nb-Ti FSS with increased chromium content. Expanding on these noteworthy properties, Kondo et al. [7] represented that in certain cases, FSS with chromium content exceeding 20% can serve as a substitute for ceramics. Nevertheless, Krishnan et al. [8] mentioned that augmentation of all required properties, including mechanical and corrosion resistance, together is the crucial and vital factor. To cite an example, tin has been discovered to be advantageous in achieving uniform corrosion resistance in acidic environments and pitting resistance in chloride-containing solutions, although it can be detrimental to the mechanical properties of stainless steel, as observed by Tan et al. [9]. However, Loto et al. [10] worked on the Ti-stabilized 430 FSS for diminishing the vulnerability to intergranular corrosion in terms of welding and/or high temperature applications. However, the grade of 430 FSS is reportedly used in various applications, namely, elevator panel, kitchenware, solenoid valve, and automobile exhaust system [11].

In terms of extensive utilization of FSS and referring to the techniques of corrosion examinations such as the electrochemical potentiostatic-based test, as a polarization technique, passivity plays a vital role because corrosion resistance can arise from the formation of the protective passive layer on the surface of such materials. In relation to the previous sections, the passivity layer reinforcement can be arisen from the presence of high chromium content leading to the corrosion resistance improvement, mentioned by Cai et al. [12] as well. Wang et al. [13] suggested that it is also important to note that different passivation behaviors can increase susceptibility to localized pitting corrosion. Likewise, to obtain pitting potential for welded, heat-treated, or other states of SS, immersion tests can be conducted, as investigated by Lei et al. [14]. Moreover, there are various studies that focus on the effect of Mo on the corrosion behavior of stainless steels, providing information about the failures induced by pitting and crevice corrosion in bromide and chloride environments. Citing another example, a study by Kaneko et al. [15] revealed that FSS exhibited better pitting corrosion resistance in bromide solution compared to chloride when the Mo content was lower than 2%, whereas the resistance was weaker with Mo content higher than 5%.

In addition, Dalbert et al. [16] evaluated the wear-out corrosion properties of AISI 430F FSS at both the surface and subsurface levels under two different passive potentials, -0.71 and -0.05 V/mercury sulfate electrode, in an acidic solution. The findings exposed that both the applied potential and microstructure can influence the oxidation growth rate, particularly affecting the subsurface microstructure of the corrosion track and resulting in a thicker, grain-refined film. Passivation, on the other hand, occurs more rapidly. In a study with non-acidic solution, De Souza et al. [17] examined the pitting corrosion and the passive film stability of the cold-rolled AISI 409 FSS sheets. The electrochemical measurements were implemented by using 0.1 molar sodium chloride solution (0.1 M NaCl) at room temperature. The general assessment of pitting corrosion was carried out by potentiodynamic and potentiostatic polarization through electrochemical impedance spectroscopy (EIS) approach while the semiconducting behavior of passive film was followed by the Mott–Schottky technique. According to their results, the grain boundaries act as the pitting initiation sites for this FSS grade. Using the same neutral as electrolyte of sodium chloride, Lei et al. [14] performed pitting corrosion criteria of a super ferritic stainless steel (SFSS), S44660, in chloride and bromide electrolytes (1 M NaCl and 1 M NaBr solutions). The curves of breakdown potential (E_b) versus temperature revealed that the pitting behavior versus temperature could be allocated three regions of transpassivation, transition, and pitting. The factors affecting corrosion resistance can be fundamentally categorized into several items such as chemical, microstructural, tribological, environmental, and other conditions. Citing an example, Jemmely et al. [18] proved that the wear-out corrosion rate of a FSS was higher in acidic solutions compared to neutral solutions due to the nature of the oxide film and the increased reactivity of the attacked surface. Rather than investigating the effect of pH value on corrosion behavior of materials due to hydrogen interaction with the surface, Landolt et al. [19] described the application of the potentiostatic technique for tribo-corrosion examinations. In other words, as pointed out by Kim et al. [20], pH variations could modify the reactivity of materials through changes in their chemistry, film thickness, and other parameters, ultimately affecting wear resistance. Indeed, potentiostatic measurements can be used to investigate this effect.

Tailoring both mechanical and corrosion resistance behavior are interconnected with the chemical composition and microstructures as also indicated by Carvalho et al. [21]. In fact, the mechanical, corrosion, and other material properties are fundamentally related to the microstructure and elemental composition of the material,

as mentioned by various studies, including Laleh et al. [22] and Jiang et al. [23]. According to a study by Li et al. [24], the properties of phases from a microstructural and textural standpoint are essential in defining the macroscopic properties, namely, processing behavior, which is a fundamental principle of materials science. To this end, Ghatei-Kalashami et al. [25] stated that the failure analysis can be controlled by the microstructural characterization that can be also interrelated to the other material properties. As a matter of fact, Liu et al. [26] verified the properties of crystalline domains determined by the defects' presence in the lattice that involves dislocations, precipitates, solute atoms, secondary phases, et cetera while a similar concept was conducted by Liu et al. [27] through another study. In this case, the dislocation density, which is one of the determinative microstructural aspects, is strongly correlated with the mechanical behavior, as indicated by Renzetti et al. [28]. Also, referring to the study by Lu et al. [29], the presence of intermetallic phases and/or secondary phases can cause undesirable degradations of the corrosion, mechanical, and other properties that is the concern of a variety of studies such as Jiang et al. [30]. This is evidently in relevance with the heat treatment temperature range as stated by De Abreu et al. [31]. According to the literature, such as a study by Shen et al. [32], hardness is frequently set as a main signifier among all other mechanical properties to model the tribological and corrosion performance in any grade of SSs.

In the current study, the mechanical and corrosion resistance behavior of annealed FSS after cold worked process has been accomplished. While the augmented strength and hardness attributed to the cold plastic deformation subjected to the cold-worked operations (e.g., wire drawing) can be significant, it is mostly essential for returning the stainless steels to its initial status through annealing heat treatment, which has been investigated by numerous studies, including a work by Bazri et al. [33]. Also, Sun et al. [34] carried out another similar study in this case. However, Liu et al. [35] and several other studies have also focused on the hot-worked materials in this regard. Likewise, Yu et al. [36] addressed its interconnection with the subsequent cooling stage as well. Annealing can decrease the hardness and strength of the cold-worked material while it can simultaneously increase the ductility reported by numerous studies such as Guo et al. [37]. This is another evidence of the challenges for the sought-after trade-off balance between strength and ductility [38]. Also, Bazri et al. [39] have stated this aspect of challenge for the classes of stainless steels. Therefore, the most significant industrial exploitation is to soften such stainless steels which are previously

hardened or rendered brittle by any cold-worked process, and for controlling of the microstructures in final products [40].

In the current research, the low-carbon and medium-chromium content FSS of EN1.4105/AISI430F is non-hardenable with enhanced machinability. However, the carbon content presents a challenge, as the higher it is, the less superior the corrosion resistance, and the lesser it is, the more non-hardenable the behavior. This grade has a relatively appropriate range of carbon content, which is allowed up to 0.12% [41]. Nevertheless, the present research focuses on the effective elements, namely, the presence of medium-content Cr and a sufficient amount of Mo, which are essential for the relevant applications.

The objectives of this study are to monitor the evolution of mechanical, metallurgical, and corrosion behavior of cold-drawn Cr-Si-S-C ferritic/ferromagnetic SS round bars after recrystallization under various annealing conditions along with two different reduction rates. The microstructures and morphologies of the wide range of designated specimens before and after recrystallization annealing were scrutinized by using the advanced approaches of electron backscatter diffraction (EBSD) and scanning electron microscope/energy-dispersive X-ray spectroscopy (SEM/EDS) to evaluate the interaction effects on mechanical and corrosion behavior. The study aims to investigate how elemental composition and metallurgical routes may affect the properties of this grade. This will optimize the industrial annealing production for the solenoid and electro valves applications in the market.

2 Experimental procedure

2.1 Materials and recrystallization annealing process

The chemical compositions of the FSS round bars, namely, EN1.4105, equivalent to AISI430F, supplied by Eure Inox srl

Company, are shown in Fig. 1. Both cold-drawn (CD) and annealed conditions of the specimens were considered for this research. Two different diameters of 9 and 11 mm, with reduction rates of 20 and 35%, respectively, were utilized. The static isothermal recrystallization annealing was conducted at three different temperature ratios of 0.65, 0.68, and 0.71, which represent the temperature ratio between the annealing heat treatment and the melting point temperatures (TRAM). In addition, the heat treatment was carried out for seven different soaking times, resulting in a total of 44 specimens with varying recrystallization fractions. The cooling stage was conducted using another furnace with an air-cooled condition at 40 °C.

2.2 Microstructural characterization method

The advanced characterization method of EBSD was utilized to scrutinize the microstructures and textures of the samples on the rolling direction (RD) plane (see Fig. 2). The EBSD processing was carried out by using an Oxford Instruments equipment, equipped with a C-Nano camera, operating at an accelerating voltage of 20 kV and a 10-nA probe current, with a working distance ranging from 15 to 18 mm, and tilted at an angle of 70°. The specimens were scanned at a magnification of 300× with a step size of 2 μm, covering the core, edge, and radial strip regions. The TANGO-CHANNEL5 software was used for post-processing calculations to determine the crystalline orientations, variations of grain and their boundaries, as well as misorientations among the neighboring detected grains.

2.3 Hardness measurements

Measurements of Brinell hardness, as the surface-based durability, were done on all heat-treated and CD samples by using an INNOVA TEST equipment under a defined load of 187.5 kgf with a 2.5-mm ball indenter and dwell time of

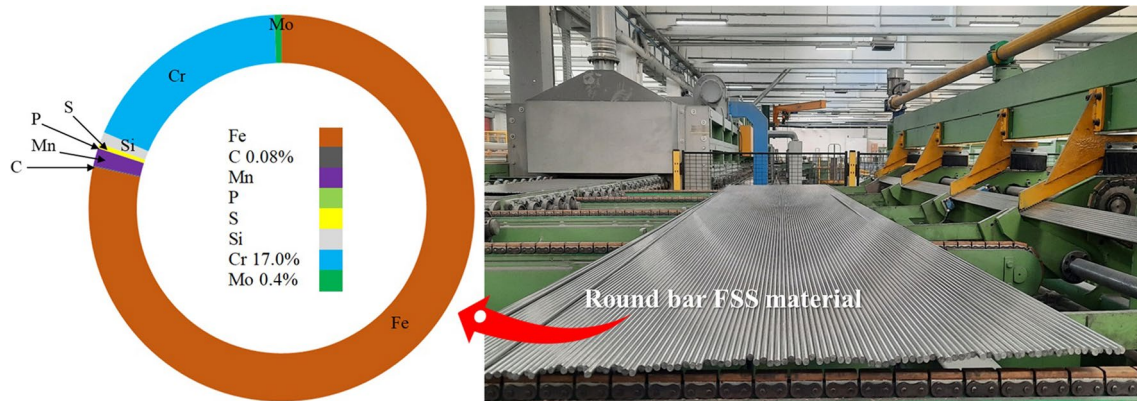


Fig. 1 Chemical composition of the chosen round bar FSS material for this study

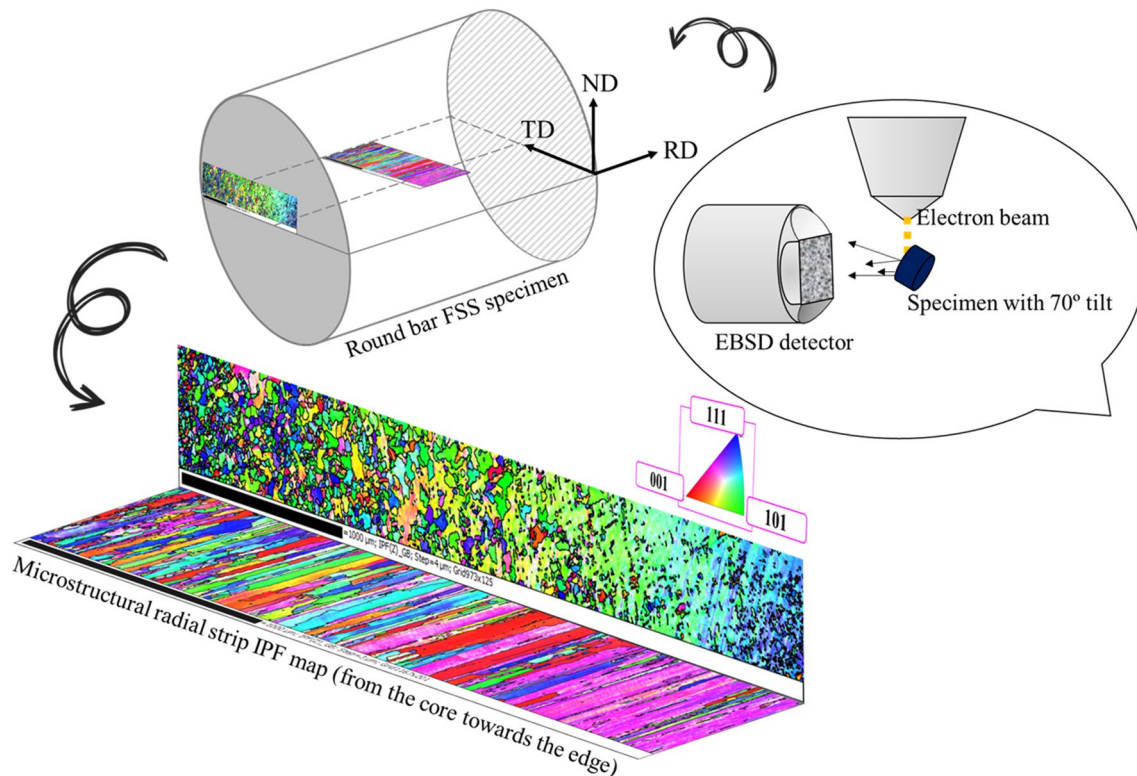


Fig. 2 The schematic overview of EBSD advanced characterization approach on the sample

10 s. The average values of five indentations were collected on each specimen.

2.4 Tensile strength measurements

The ultimate tensile strength (UTS) (R_m), 0.2% offset yield strength ($R_{p0.2\%}$) (0.2OYS), and total elongation (TE) were determined by mechanical tensile examinations by using an INSTRON 3382 machine with a capacity of 100 kN and a cross-head speed of 0.04 mm/s at standard room temperature. The minimum length of the test pieces was 150 mm, in accordance with the standards. For such a destructive test, it is necessary to separate the samples from the pieces intended for magnetic, corrosion, and microstructural examinations. Apart from the regular procedure, several standards permit the test without doggy-bone machining, including ASTM A962/A 962/M, ASTM A370, EN ISO377, ASTM E8, and EN 10002–1. For instance, ASTM A370 indicates that the mechanical tensile test of steels can involve a full section of the bar materials. EN ISO377 specifies that full-section test specimens can be used as long as the testing equipment and machining are suitable. Likewise, ASTM E8 mentions that the test pieces can be substantially full-section. Lastly, EN 10002–1 indicates that bar specimens of full cross-section can be tested without being machined.

2.5 Electrochemical corrosion examinations

In this study, the susceptibility of localized (non-uniform) pitting corrosion and the structural general (uniform) corrosion, through the passivation and repassivation mechanisms of EN1.4105/AISI430F FSS, were investigated by using potentiostatic technique, considering SEM-based morphology and concerning the microstructural evolution. This approach defines very accurate computations of corrosion resistance of stainless steel by providing the polarization curve. The approach of extended variant of double loop electrochemical potentiostatic repassivation (DL-EPR) was aimed for the pitting and general corrosion analyses. The polarization curves were obtained by using a glassy three-electrode equipment connected to a potentiostat called Amel, an electrolytic-cell-based equipment where the specimen was fully immersed in an electrolyte solution. The cell consisted of a targeted FSS specimen shaped as a small round disc (with a minimum exposed surface area of 82.47 mm² to the electrolyte solution) of 5-mm thickness as the working electrode, platinum as the counter electrode, and a calomel electrode (Hg₂Cl₂) as the reference electrode, which is a material that is highly stable under the test conditions and was employed to monitor and maintain the potential at the surface of the working

electrode. The selection of the most extreme conditions of the samples took into account for corrosion examinations, microstructural observations, and mechanical tests. All pre-defined heat-treated and as-built CD round bar samples were precisely cut into the test pieces. The specimens were ground using silicon carbide (SiC) emery/abrasive papers of 320, 600, and 800 grit. Ensuring the identical surface quality of all specimens was truly organized to enable their comparison within the corrosion examinations. In addition, the flatness of the sample's surface was critical for these tests and was carefully controlled during surface preparation. Two solutions, 1.0 M sodium chloride and 1.0 M sulfuric acid, were used in stagnant conditions and at standard room temperature for the experiments. For this FSS grade and in the case of sodium chloride electrolyte solution (SCES), corrosion is expected to be initiated by the presence of negatively charged chloride ions (Cl^-), which is able to accelerate corrosion by promoting plausibly other sorts of reactions, namely, formation of chlorides, direct attack, and the localized corrosion. From an experimental standpoint, the test solution was freshly prepared to avoid any inaccuracies, and the required electrodes were cleaned using an abundant-enough water bath at the required temperature (± 1 °C) for each examination. The tests were duplicated and repeated to reduce uncertainties.

The potentiostatic tests were carried out from potentials -800 to $+2000$ mV with a step potential of 0.1 mV and from the current range of ± 10 nA to ± 1 A for time duration of 2 h. Based on typical Tafel-based plots of potential versus $\log I$, if the potential moves through the positive direction, the anodic behavior is shaped, and, conversely, it would be a cathodic polarization if it sweeps away in the negative direction. For the potentials lower than the defined corrosion potential (E_{corr}), the material is corrosion protected, which is the cathodic behavior, whereas for the potentials greater than E_{corr} , the material is oxidizing as the anodic behavior. In this case, the passivation could start, and its potential indicates division of the decreasing current from the increasing side on the curve. Pitting corrosion value (E_{pit}) signifies the onset potential level in which the provided protection by the passive oxide film is vanished due to the phenomenon of trans-passivation or the localized breakdown and failure of the oxide which delineates the pitting zone. The more superior the pitting potential of the material, the higher the localized corrosion resistance. Also, the after the stable pitting growth is pointed out to the breakdown potential (E_b), depending on the curve behavior and addressing the potential level at which the current density specifies a sharp upsurge. In this study, the following parameters were designated: the corrosion potential, E_{corr} , primary passivation potential at which

the passive surface layer would be formed, E_{pp} , which also defines the critical current density or the primary passive current density, i_{cr} , passive potential, E_{pa} , pitting potential corresponding to the end of passivity region, E_{pit} , the secondary passivation potential, E_{sp} , and the oxygen evolution potential, E_{oe} , following the repassivation loop, all also corresponding to the relevant current densities.

3 Result and discussion

3.1 3.1. Mechanical analysis: tensile strength and hardness

Figures 3 and 4 illustrate the stress–strain curves obtained for all series of CD and heat-treated samples, while Table 1 represents the results of all measured tests. Over the results of mechanical tensile strength examination, it could be demonstrated that, in general, the maximum and minimum values for three significant parameters of the UTS, 0.20YS, and TE have been obtained at the minimum and maximum annealing incubation time (AIT), respectively, addressing each set of annealing soaking temperature (AST). In this case, the maximum range of UTS among heat-treated materials was observed at 0.65TRAM AST and 5 min AIT for 20% RR; however, the maximum of elongation has been gained at 0.71TRAM AST and 640 min AIT for 35% RR. In other words, the more AIT increased, the less tensile strength values (also specifically compared to CD sample) were achieved over the defined interval time that approved the non-hardenable behavior of the present grade.

In contrast, and compared to the CD samples, an approximate diminished value of 100 and 197 MPa in UTS along with an 84.5 and 279.2% raising in the TE for the annealed specimens with 20 and 35% RR were obtained, respectively, that demonstrated the improved mechanical behavior based on this targeted non-hardenable grade.

Furthermore, in order to decide the optimum scale for recrystallization annealing, apart from the mechanical behavior implications, it is quite substantial to appraise the other properties, such as corrosion and metallurgical owing to the microstructural and textural considerations alongside the reduction rate of the materials for an accurate decision. This is the hypothesis of the current research, which has been carried out.

Likewise, the decline in hardness was driven by the annealing of cold-worked samples similar to the tensile strength behavior. Following Fig. 5, the local hardness diminished in comparison to the base CD unheated materials that again was in good agreement with the behavior of targeted non-hardenable materials to meet the industrial applications required.

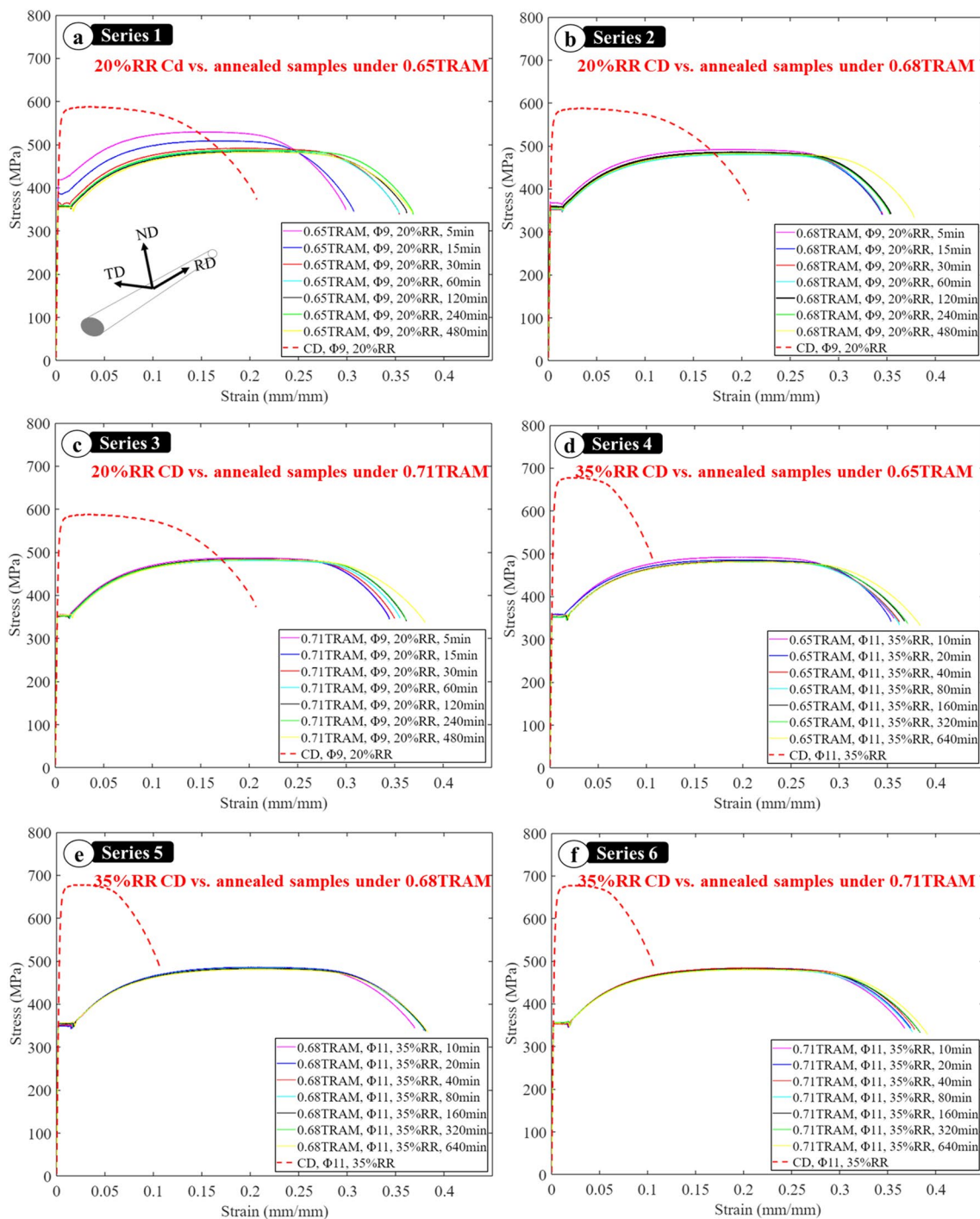


Fig. 3 Overview of the output results of mechanical tensile strength tests while the annealing incubation time was pivoted by the comparison graphs

3.2 Surface morphology analysis of tensile fracture

The SEM-based macrostructure of the CD sample by 20% RR revealed a central propagating fracture line

surrounded by satellite cracks, indicative of strain localization and initial microvoid coalescence (observing at 35X magnification in Fig. 6a). Figure 6b shows that the microstructure exhibited a network of microvoids, among

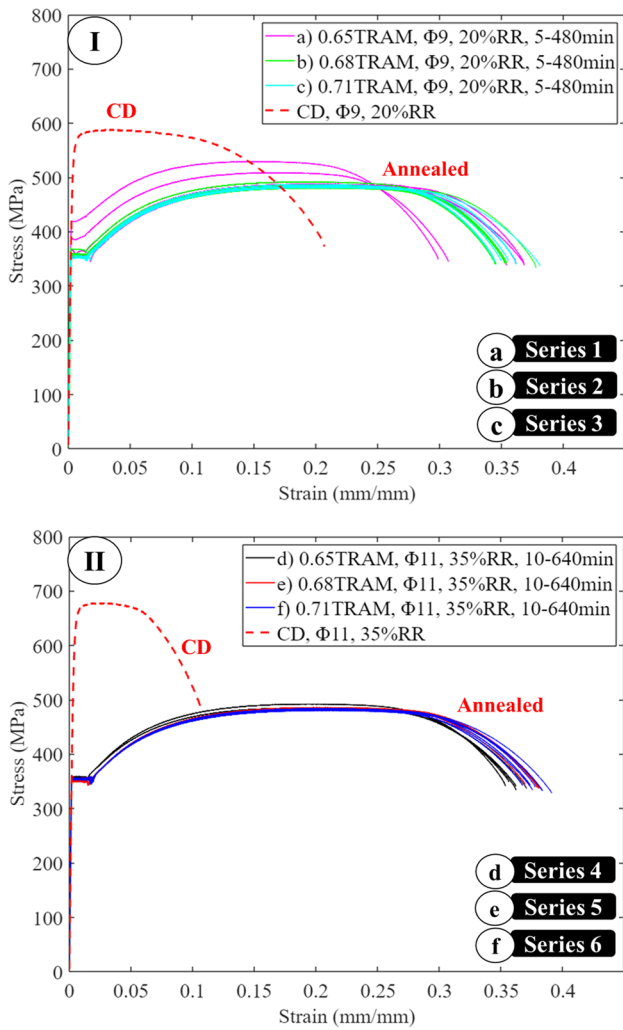


Fig. 4 Overview of the output results of mechanical tensile strength examination while the AST was turned by the comparison graphs, for (I) 20% RR and (II) 35% RR, specifying variation of CD and annealed materials through the tensile strength test, corresponding to the original deformed grains versus the grains evolution phenomenon

an interwoven connectivity portraying a typical ductile fracture surface with the intergranular connectivity. Such an intergranular connectivity described the networked pattern of microvoids, emphasizing the interlinking nature of the typical ductile fracture process. According to Fig. 6c, for the sample with 20% RR under 0.65TRAM within 480 min AIT, a microstructural refinement was apparent, with the presence of minute, distributed microcracks after the material is almost fully recrystallized. Smaller microvoids were shown in the more cohesive, interwoven manner, suggesting a controlled ductile rupture process in Fig. 6d.

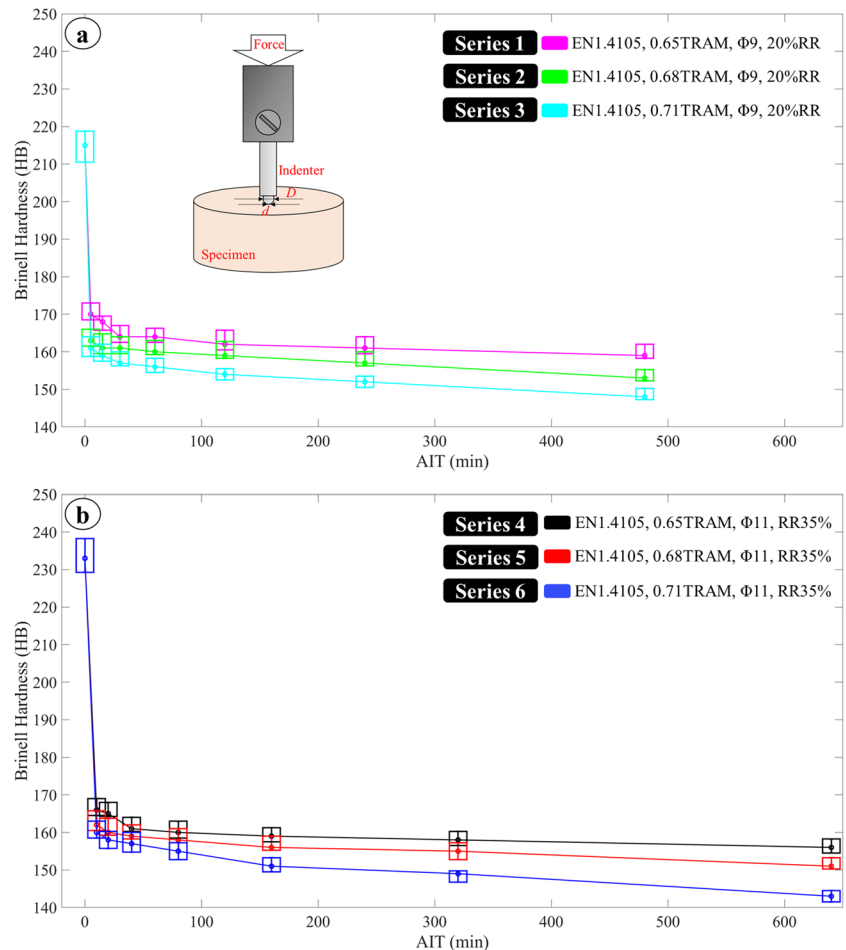
For the CD sample by 35% RR, the fracture pattern exhibited macroscopically a distinct clock-like configuration, indicative of the more profound level of deformation and stress concentration during the cold-drawing process, as illustrated in Fig. 6e. The microscale in Fig. 6f revealed an ensemble of larger microvoids in comparison to the CD sample by 20% RR, arranged in such interconnected pattern, underscoring the ductile mode of fracture. As for the sample with prior 35% RR under 0.65TRAM of AST within 320 min AIT, the fracture surface at 35X magnification disclosed two prominent major cracks accompanied by the network of minor microcracks, emphasizing the effect of annealing after cold-worked process. In addition, microvoids in Fig. 6h, presented in the interwoven arrangement, highlighted the ductile mechanism.

Overall, the smoother surfaces and highly reduced plastic deformation at higher AST indicated the recovery and recrystallization process, which tended to reduce the effects of cold working. Moreover, there is a general transition from larger cracks to the smaller ones alongside more uniform dimples and the change in surface morphology specified a shift from the less ductile to the more complete ductile fracture mechanism after annealing.

Table 1 The measured mechanical tensile tests of cold-drawn and annealed specimens

Specimens	UTS, R_m (MPa)		0.2OYS, $Rp_{0.2\%}$ (MPa)		Total elongation, TE (%)	
	Max	Min	Max	Min	Max	Min
Φ9 mm, 20% RR, CD	587	–	548	–	20.7	–
Φ9 mm, 20% RR, 0.65TRAM	529	483	418	354	37	30.05
Φ9 mm, 20% RR, 0.68TRAM	492	483	367	355	38.3	34.4
Φ9 mm, 20% RR, 0.71TRAM	487	483	355	351	38.2	34.9
Φ11 mm, 35% RR, CD	677	–	632	–	10.6	–
Φ11 mm, 35% RR, 0.65TRAM	492	482	358	350	39.6	35.6
Φ11 mm, 35% RR, 0.68TRAM	485	481	356	353	39.8	38.9
Φ11 mm, 35% RR, 0.71TRAM	484	480	359	353	40.2	38.5

Fig. 5 Overview of the results of the Brinell hardness tests versus the AIT, considering the AST as well, variation of CD and heat-treated materials in Brinell hardness, (a) for the series with 20% RR, and (b) for the series with 35% RR



3.3 Secondary phase identification on tensile fracture surface

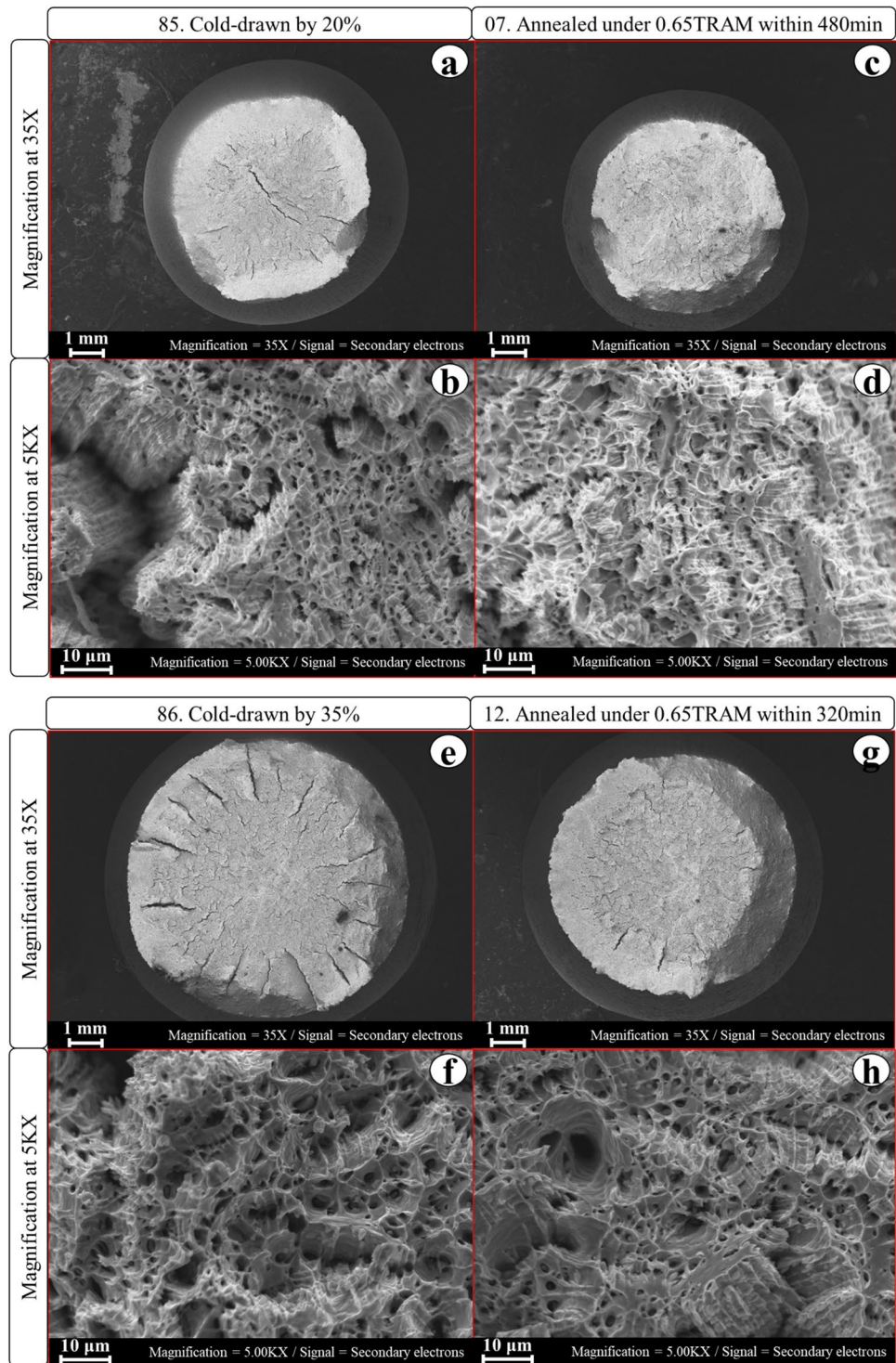
Figure 7 depicts the SEM/EDS analysis of tensile fracture surfaces for the identification of the secondary phases, considering their demonstrated chemical compositions. Figure 7a for the CD specimen No.85 with 20% RR detected the Cr-rich phase on the spotted particle, given the high chromium content. Cold drawing has induced strain and plastic deformation, promoting the formation of such chromium-rich secondary phases due to the redistribution of alloying elements. However, further X-ray diffraction (XRD) analysis would be required for more accurate and reliable determination of these secondary phases, as the crucial contributors to the material properties such as mechanical behavior. Based on Fig. 7b corresponding to sample No.07, the presence of spotted sulfur and manganese hinted the formation of manganese sulfide (MnS), as a common inclusion in steels. Indeed, the conditions during recrystallization annealing could facilitate the precipitation of such manganese sulfide

inclusions. Likewise, in Fig. 7c, the high manganese content of the CD sample No.86 indicated the possibility of the manganese-rich secondary phase, potentially an intermetallic compound. In fact, the increased RR, as the higher degree of deformation, could be the driving force to promote such formation of manganese-rich secondary phases. Lastly, according to Fig. 7d of annealed sample No.12, the presence of sulfur and manganese indicated MnS formation. However, such combination of Cr and Mn could also suggest the formation of a chromium–manganese intermetallic phase. All these samples were analyzed by XRD for further identification in more details.

3.4 Secondary phases identification by XRD analysis

In this section, the focus has been on the identification of secondary phases by XRD analysis. Through the investigations on tensile fracture surfaces, the synergy between EDS and XRD was found essential for scrutinizing the presence of secondary phases. While XRD can provide a

Fig. 6 SEM-based fracture surface morphology of CD sample by 20% RR at magnifications of (a) 35X and (b) 5000X, the sample under 0.65TRAM of AST within 480 min AIT with prior 20% RR at (c) 35X and (d) 5000X, CD sample by 35% RR at magnifications of (e) 35X and (f) 5000X, the sample under 0.65TRAM of AST within 320 min AIT with prior 35% RR at (g) 35X and (h) 5000X



more extensive view of the crystalline phases in comparison to EDS, offering more localized chemical perceptions, such combined approaches can promise detailed understanding. Combining EDS results with the obtained data by XRD plots was the more precise approach to identify the secondary phases. According to Fig. 8a of specimen No.85, apart from the dominant peaks contributing to

the main ferritic matrix as the characteristic of the bcc crystalline, the other peaks at 34.93, 40.78, and 72.40° indicated the chromium-rich intermetallic carbides. The process of cold drawing by inducing strain and plastic deformation has facilitated the development of secondary phases enriched with chromium. This occurrence has been the result of the redistribution of alloying elements. For

Fig. 7 Revealing SEM/EDS analysis of tensile fracture surfaces for secondary phase identification and their chemical composition elucidation: (a) CD sample by 20% RR, (b) the sample under 0.65TRAM of AST within 480 min AIT with prior 20% RR, (c) CD sample by 35% RR, (d) the sample under 0.65TRAM of AST within 320 min AIT with prior 35% RR, and (e) the results of EDS analysis

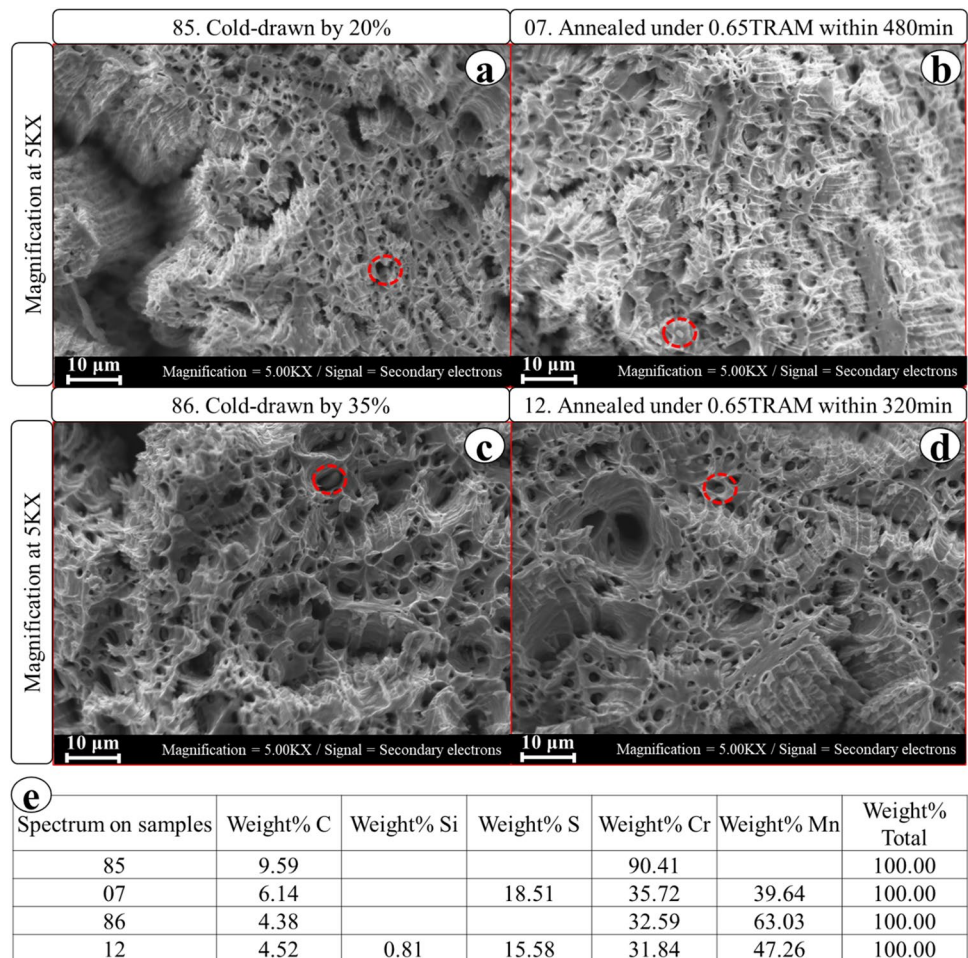


Fig. 8b of annealed specimen No.07, the peak at 34.46° pointed to potential chromium-rich intermetallic phases or carbides, and, because of EDS-based results, the reasonable interpretation emphasized the presence of chromium carbides again. The same analysis could be implemented at 61.86° while any additional investigation by more accurate techniques such as transmission electron microscopy (TEM) can emphasize the need for further analysis. In Fig. 8c, peaks at 34.34 and 40.01° specified potential chromium-rich carbides while the 43.02° peak suggested a secondary phase requiring further scrutiny as well. In a similar scenario, Fig. 8d exhibits potential chromium-rich carbides at 34.12° , linking to the results of EDS as well. Overall, the EDS results underscored the complexity of secondary phases in this FSS material with different conditions. However, the more in-depth combined analysis by XRD revealed the precise identification and characterization. These findings laid the groundwork for the comprehensive understanding, crucial for optimizing the mechanical and corrosion-resistant properties of this FSS grade.

3.5 Effect of microstructures on mechanical behavior

The microstructures developed in the CD specimens after annealing must be scrutinized to understand the variations in annealing conditions implemented by different soaking temperatures and incubation time. However, such a characterization of microstructures comprised numerous EBSD maps. This study featured average grain size (AGS), grain boundary (GB), nucleation, and dislocation density (DD) into the investigation of mechanical properties and corrosion behavior. The phase map was observed by fully ferrite domain while it was based on the recrystallization annealing without phase transformation. Aforementioned varied mechanical results were definitely arisen from various microstructures. Overall, in this research, the focus on microstructural investigation was accomplished on the core region of samples. The critical zone was assigned in the center because the preceding grain evolution is evidently occurred on the edge, following the surface exposure to the heat treatment.

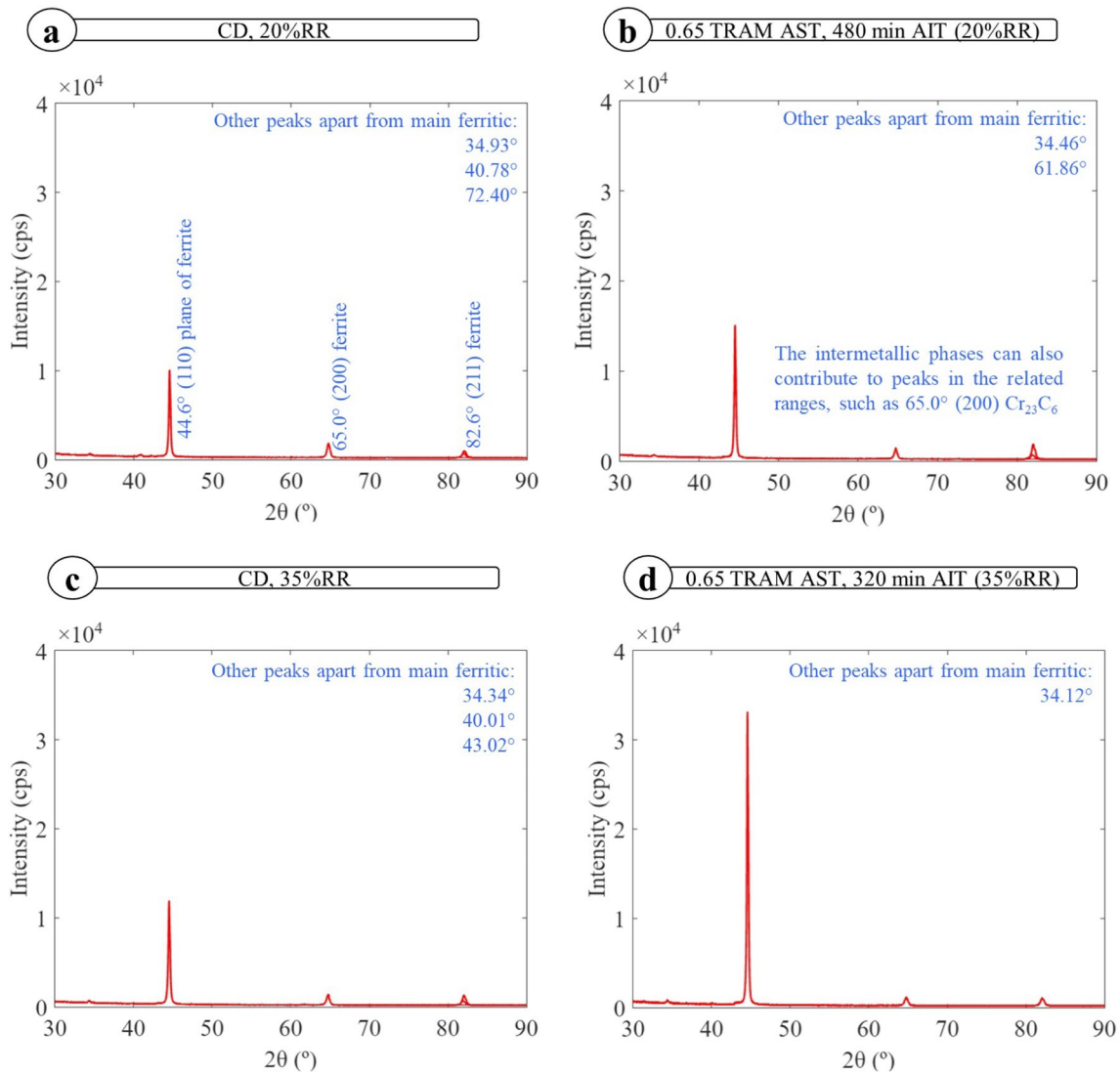


Fig. 8 XRD analysis of (a) CD sample No.85 with 20% RR, (b) sample No.07 under 0.65TRAM of AST within 480 min AIT with prior 20% RR, (c) CD sample No.86 with 35% RR, and (d) sample No.12

under 0.65TRAM of AST within 320 min AIT with prior 35% RR, all addressing as the typical intensity (counts per second (cps)) as a function of the XRD scan range of 2θ ($^{\circ}$)

The mechanical behavior is obviously directly attributed to the microstructural characteristics. For these specimens, EBSD-based AGS ranged from 50.59 to 86.18 μm for 20% RR and from 27.02 to 40.52 μm for 35% RR. The corresponding decline in hardness was 32.1 and 39.06%, respectively, with a 17.7% and 29.1% decrease in UTS. In other words, the hardness of the CD samples was approximately 47.3 and 64.1% higher than those of fully recrystallized samples for 20 and 35% RR, respectively. Similarly, the UTS values were measured to be around 21.5% and 41.1%, respectively. The AGS in the as-received bars was detected 53.50 and 27.02 μm for $\phi 9$ mm with 20% RR and $\phi 11$ mm with 35% RR, respectively. Growth in the grain size caused the decline in the yield strength limit because

the broader grain boundaries were not completely able to restrict dislocations sliding, as also referred to the literature [42]. This has been exactly vice versa during cold wire drawing process while the higher quantity of dislocations within any of the grains would be activated to enable cold deformations throughout the neighboring grains. To this end, while the soaking temperature increased, the grain size trend would be the key microstructural mutation in the materials, leading to a decline in mechanical tensile strength and hardness characteristics of this body-centered cubic α -ferrite grade. In the meantime, a noticeable upsurge in the elongation was related to the recrystallized grains in comparison to the unheated material even with incomplete recrystallization. In other words, the ultimate ultrafine

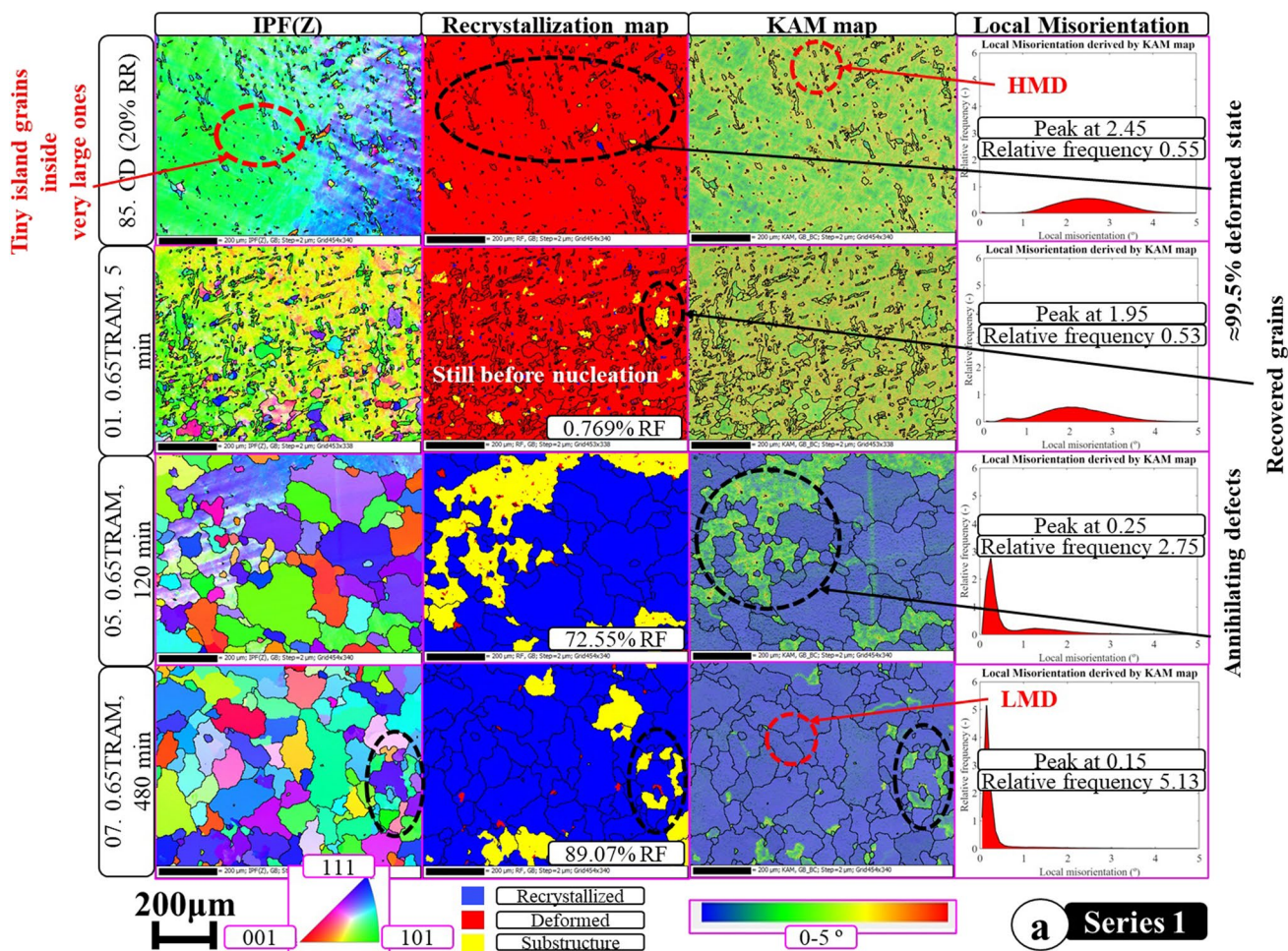


Fig. 9 Microstructural maps, including IPF, recrystallization, and KAM maps of all different designated annealing conditions versus their unheated states: (a) 0.65TRAM, ϕ 9 mm, 20% RR; (b)

0.68TRAM, ϕ 9 mm, 20% RR; (c) 0.71TRAM, ϕ 9 mm, 20% RR; (d) 0.65TRAM, ϕ 11 mm, 35% RR; (e) 0.68TRAM, ϕ 11 mm, 35% RR; and (f) 0.71TRAM, ϕ 11 mm, 35% RR [44]

equiaxed grains of this ferrite triggering the improvement of the mechanical properties owing to the lattice close-packed structures, attributed to the targeted non-hardenable FSS. Referring to the current industrial cold wire drawing processing, some percentage of the expended energy is stored in the material that leads to an increase in internal energy, which is accordingly associated with an increase in DD. In other words, the dislocations arise from the thermodynamic driving force of internal energy. Likewise, the dislocation density increases at higher scales of cold-worked deformation, which is associated with an increment in residual stresses.

In general, the approaches for local misorientation (LM) investigation in the deformed and the subsequent annealed microstructures involve kernel average misorientation (KAM), grain average misorientation (GAM), and grain orientation spread (GOS) [43]. KAM method has been used in

this work to represent the LM among neighboring grains, as a collective of dislocations in each grain. Figure 9 displays the KAM maps, overlapped with the GBs, where respective to the colors from blue toward red, the KAM values of misorientations were signified from 0 (minimum misorientation) to 5° (maximum misorientation), as for the reference interpretation to the colors. In fact, the KAM maps of the same area for inversed pole figure (IPF) and recrystallization fraction (RF) maps were visualized in Fig. 9 to scrutinize the pattern. A misorientation angle, which was detected higher than 15° ($\theta > 15^\circ$) among the adjacent grains, regulates the high-angle grain boundaries (HAGB), and, subsequently, the low-angle grain boundaries (LAGB) or the subgrain boundaries were set by $\theta < 15^\circ$. To be precise, the misorientation angles between 2°, as the internal misorientation, and 15° were set as the subgrain domains, which are building up during recovery.

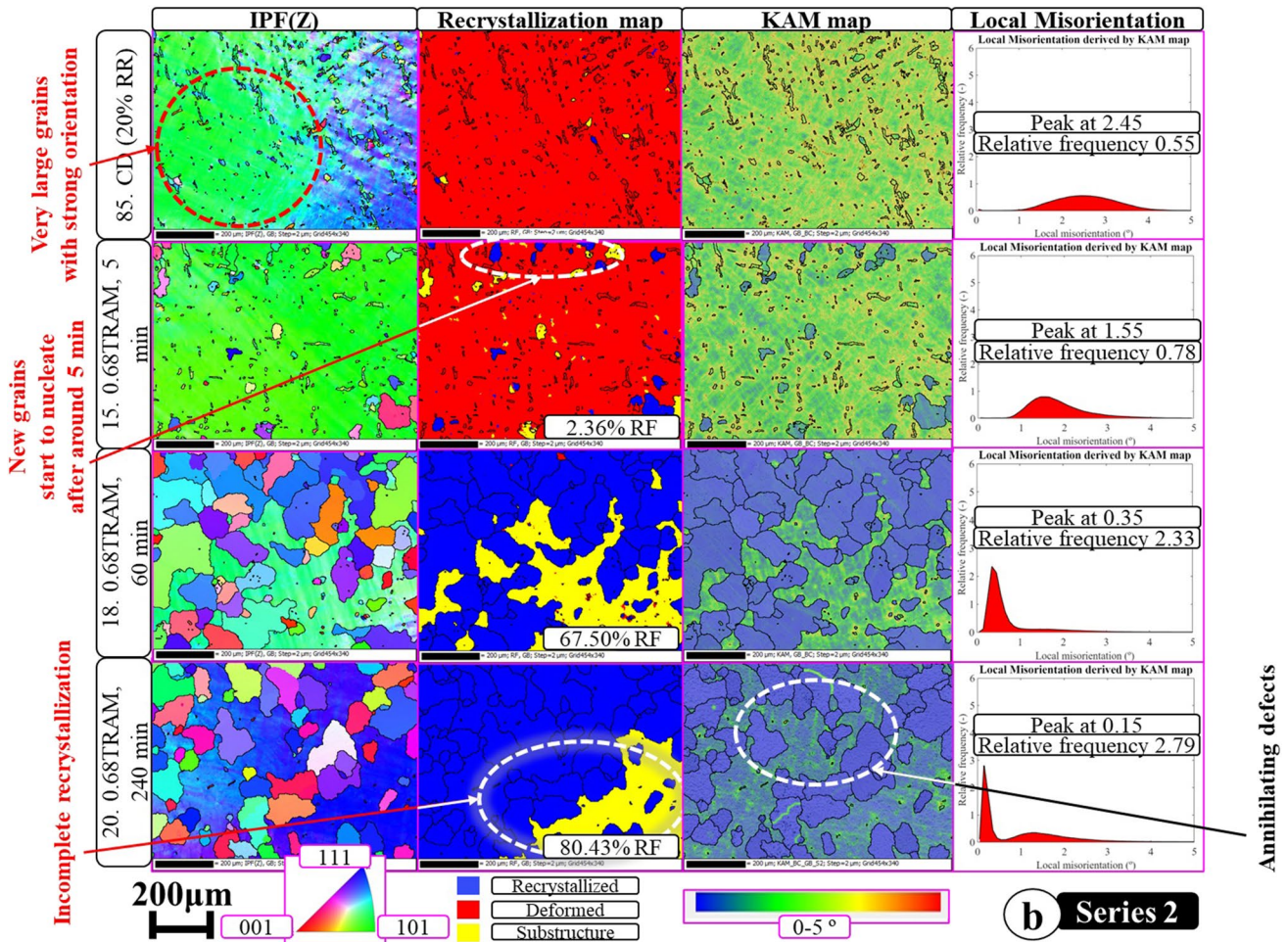


Fig. 9 (continued)

On the other hand, by increasing the AST, the quantity of HAGBs was increased as well while LAGBs were decreased (Fig. 10). Through migration of boundaries, dislocations accumulated continuously, shaping the dislocation walls and subgrains by reaching GBs. Recrystallization occurred while LAGBs transformed into HAGBs at critical DD through this process, leading to the formation of new grains. At the same time, dislocation movements speeded up the annihilation of dislocation. Such microstructural phenomenon ultimately causes the LAGBs to decline and increases the average misorientation. Figure 11 demonstrates that the lower LM angles at higher relative frequencies have been achieved by increasing the AST and AIT, for example, from 2.45 to 0.15° for 20% RR and 3.15 to 0.15° for 35% RR when the AST increased from 0.65TRAM to 0.71TRAM, and the AIT generally increased from 5 min to more than 10 h (640 min) for various series of annealing conditions.

Regarding dislocation densities, the CD specimens showed the worst LM of 3.15 and 2.45°, whereas the high-recrystallized samples exhibited the best and lowest misorientations of 0.15°. It is evident that the more recrystallization has addressed the minimum misorientations with higher relative frequencies. As for the mechanical behavior, such higher local misorientations could be attributed to higher internal strain, affecting bonding of the lattice structures, which also causes the higher resistance of dislocation activities around the grain boundaries, engendering lack of adequate mechanical properties.

Figure 12 illustrates the variations of ultimate tensile strength values versus the AGS as the function of annealing time. The mechanical tensile strength enhanced in terms of non-hardenable FSS with increasing AGS of 50.59 to 90.50 µm as well as 27.02 to 48.90 µm for 20% RR as Fig. 12a and for 35% RR as Fig. 12b, respectively. It was observable that except for the 0.65TRAM of 20%

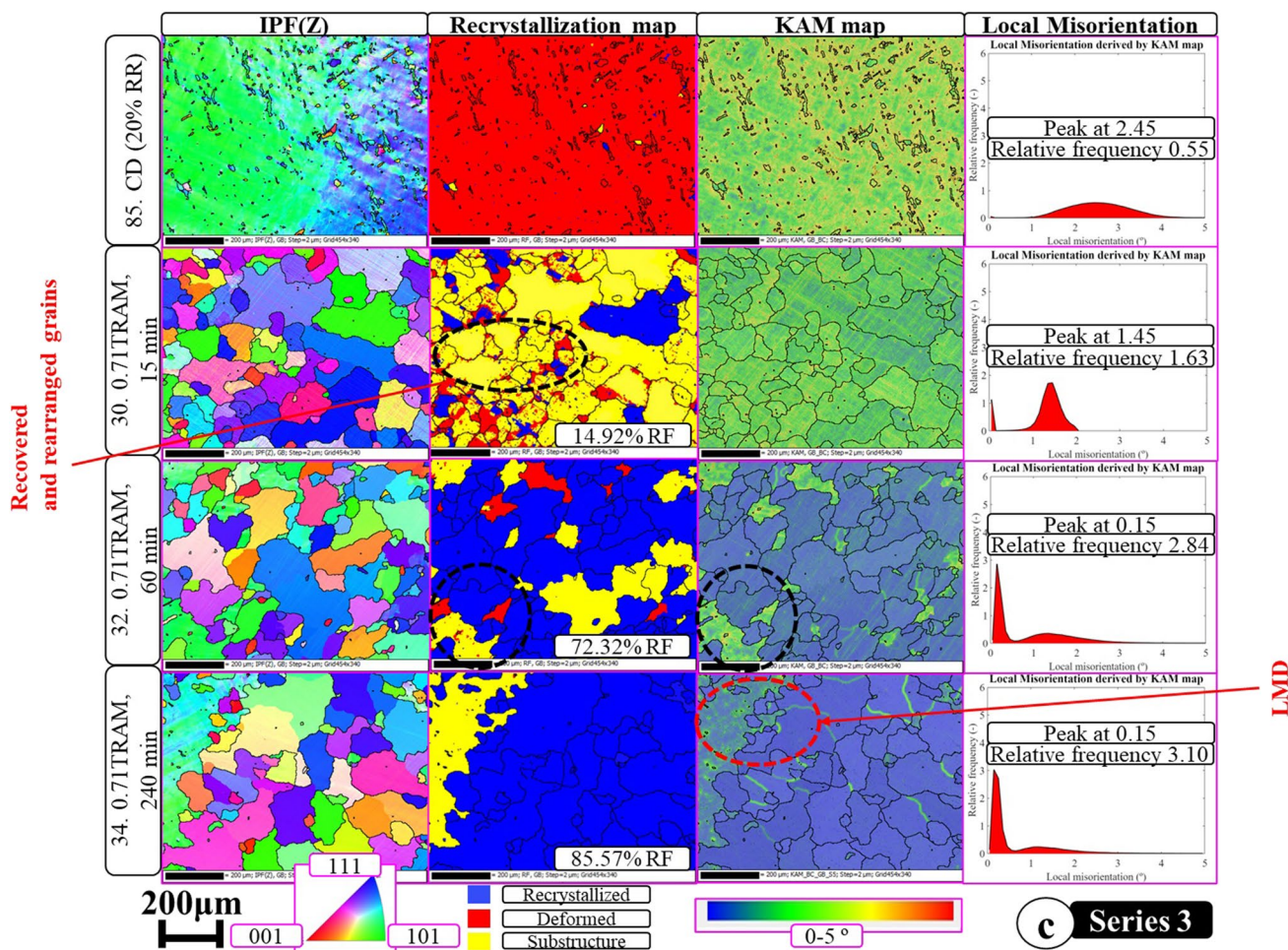


Fig. 9 (continued)

RR, which is a bit harder material among minor recrystallized, all the other mechanical tensile strengths could be quite acceptable in respect to the final product required. In other words, the adjustable average soaking temperature with enough incubation time for recrystallization could be applicable for the annealing process, avoiding the usage of more energy. However, such decision could be trustable after appraisal of corrosion tests as well. It was also evident that the material with higher RR behaved with larger tensile strength and smaller grain sizes due to the higher cold deformation stage.

In another standpoint, the pertinent mechanical properties of UTS trend as opposed to the elongation trend as a function of AST and AIT and by considering the microstructures, which has been illustrated here only for the series 1 with 0.65TRAM of 20% RR, but for all specimens of 20 and 35% RR, are shown in Fig. 13a, pointing out from CD to different annealing conditions. In this regard,

the overall region of non-hardenable can be delineated to distinguish from the medium hard material after cold working condition as well. Figure 13b depicts the quartile-based Brinell hardness trend as a function of AIT for the series 1 for better understanding of the aforesaid targeted non-hardenable FSS.

In conclusion of this section, the mechanical properties of this FSS grade were profoundly influenced by microstructural variations, specifically AGS, GBs, nucleation, and DD, resulting from diverse annealing conditions. A direct correlation was observed between increased AGS and a decline in yield strength, attributed to broader GBs impeding dislocation sliding. Conversely, during cold wire drawing, smaller AGS were associated with enhanced mechanical properties due to increased dislocation activation. Regarding the annealing parameters, higher optimum AST of 0.71TRAM and higher suitable AIT (before excessive grain growth) facilitated lower

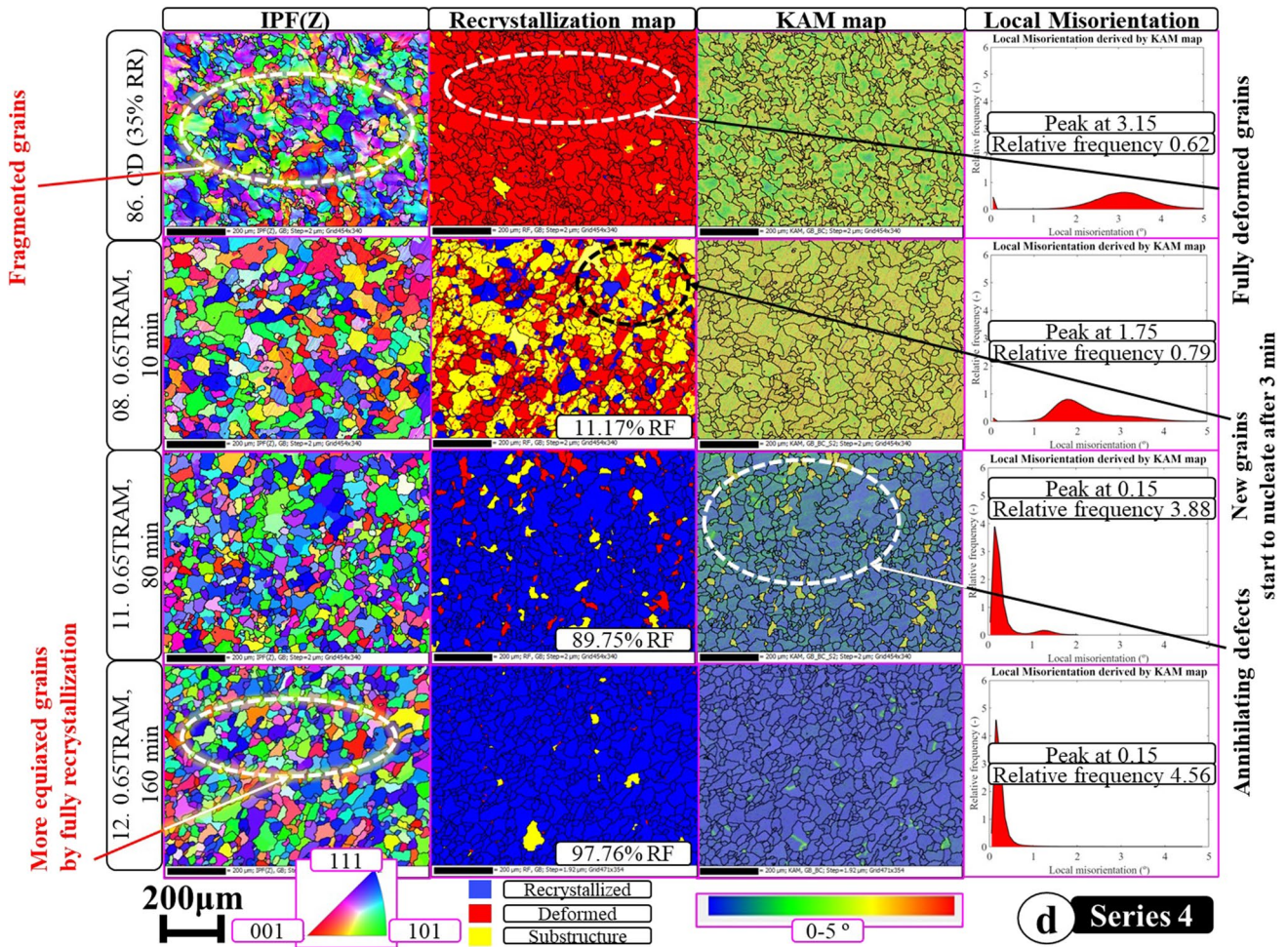


Fig. 9 (continued)

local misorientation angles, indicative of reduced dislocation densities. The mechanical response, illustrated through UTS trended and elongation, highlighted the influence of annealing conditions on achieving desired non-hardenable characteristics. Therefore, this can be directly associated with the required properties of the application; for instance, considering the energy consumption, even 0.68TRAM AST was found to be optimized in the case of mechanical properties as a very close range to 0.71TRAM results.

3.6 Corrosion resistance evaluation

3.6.1 Passivation layer formation in sulfuric acid electrolyte solution

The potentiostatic-based polarization curves in terms of different CD and annealed specimens are illustrated in this

section, recorded in 1.0 M sulfuric acid electrolyte solution (SAES) after 2 h of immersion and at standard room temperature, addressing different regions of polarization curve, which were previously explained. All specimens exhibited almost a wide stable passivity region, corresponding to formation of a protective film on the surface. Nevertheless, almost all cases showed the passivity breakdown happening (with different intensities) in this corrosive medium, provoking either sharp or smooth upsurge of the anodic current. In the actual situation, this can be where it causes rapid dissolution leading to the material failure. The dissolution can come up by either breaking the passive film causing localized corrosion or by vanishing it totally. To clarify, passivity is a dynamic stage where the oxide formation and oxide dissolution take place at the same time. The passivity is assumed as a steady state with the low rate of dissolution, while passivity breakdown happens if the dissolution goes faster than the formation.

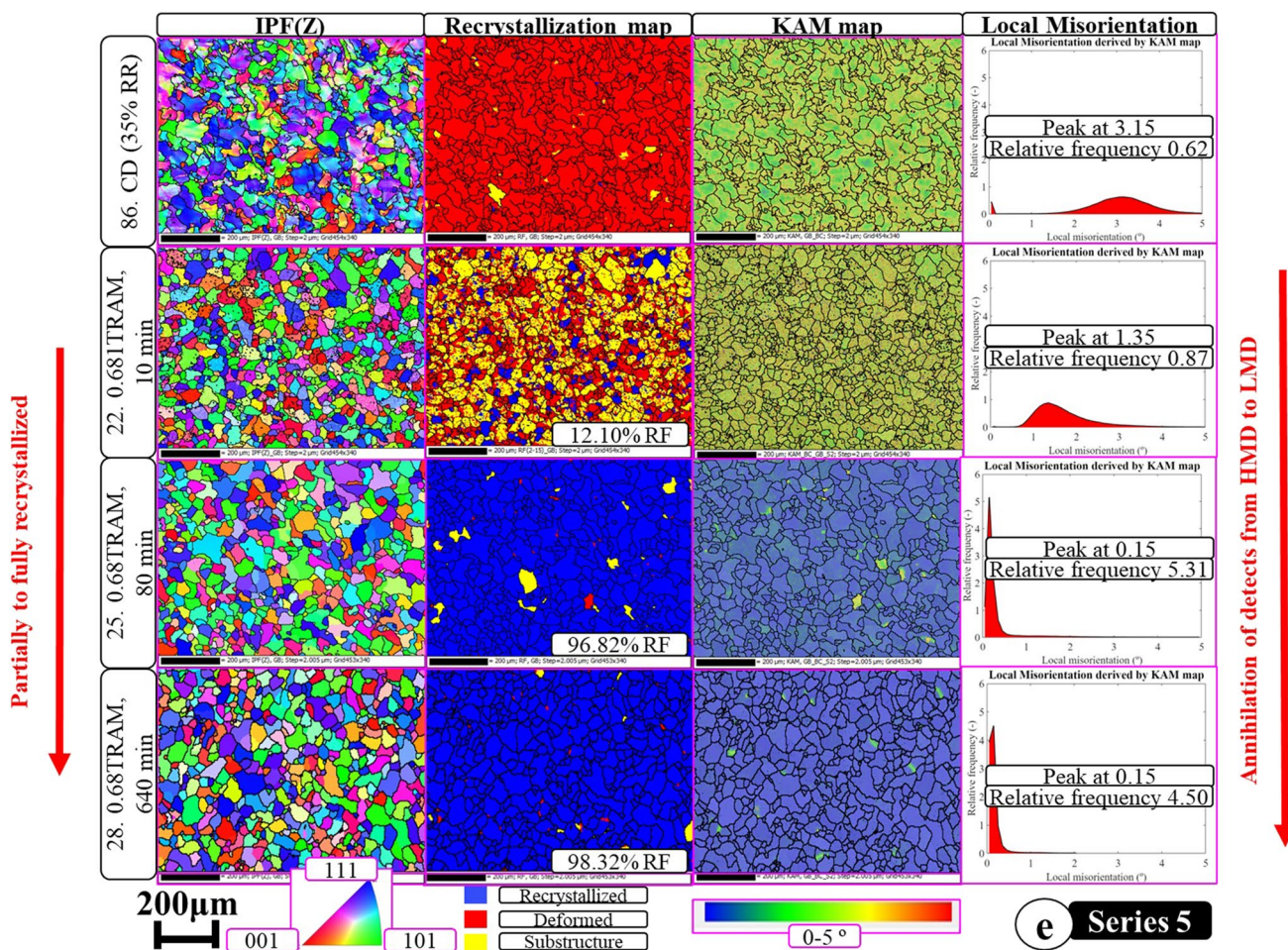


Fig. 9 (continued)

However, in this study, a sort of secondary passivation could be observed through transpassivity regime, and consequently the occurrence of oxygen evolution has been the final targeted stage. In other words, it must be noted that after the passivation region, the pitting corrosion was balanced by the new passivation layer, which also could be interpreted by the very weak secondary passivation for some of the specimens although still such current density was observed almost as high as the maximum/critical current density. By observing the oxygen evolution regime, the potential (voltage) was swept in the reverse direction after initially undergoing the forward scan. The material underwent a similar transition in the reverse direction. The intersected points of the reversed scan loop with the forward scan loop provided the repassivation potential for further understandings. To compare all the samples referring to the passivation criteria, Fig. 14a and b show the polarization

curves for the specimens with 20 and 35% RR by considering the values of passive potential and passive current density. As can be observed, the CD specimens exhibited the highest passive current densities of $2.01e-04$ A and $6.65e-04$ A for 20 and 35% of RR, respectively, among each series. This was also very noticeable that the material with higher reduction rate showed less resistance to the corrosion, specifically pitting corrosion. Subsequently, Fig. 14c and d illustrate the reverse scan loop for further analyses of complete and incomplete passivation, pointing out the intersection between two loops. These figures depicted both passivation and repassivation (as the extended variant of double loop electrochemical potentiostatic repassivation (DLEPR)) to scrutinize the aforesaid complete and incomplete passivation through the intersected point of two loops (Table 2). However, it is important that these quantitative scales of electrochemical corrosion results were concerned

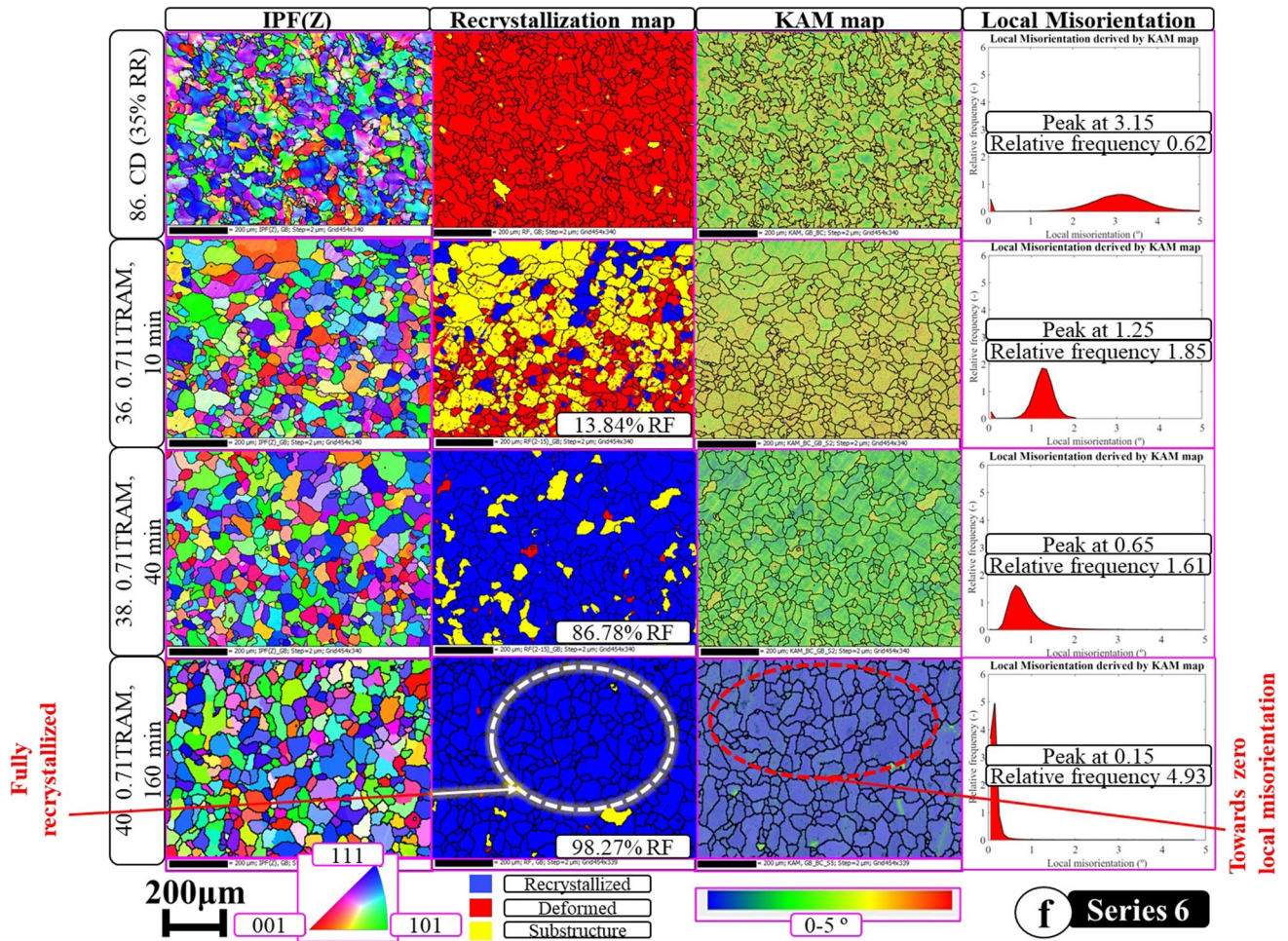


Fig. 9 (continued)

to the microstructures, chemical composition, concentration of test solution and its temperature, along with other parameters.

In conclusion of this section, the first priority for stronger resistance of such a FSS grade to pitting corrosion inside such an acidic solution has been revealed by the lower reduction rate. In other words, the lesser the reduction rate, the higher the corrosion resistance. The second factor has been found by the AST. To clarify, the higher corrosion resistance was attributed to the higher annealing temperature. The third effectual item was concluded by the AIT. It means that higher annealing time addressed also higher corrosion resistance.

3.6.2 Active anodic behavior in sodium chloride electrolyte solution

Similar to the previous section, the potentiostatic polarization curves are shown in Fig. 15 for the chosen specimens in 1.0 M SCES after 2 h of immersion and at room

temperature. However, the main difference lay in the distinctive tendency to be active in this environment containing sodium chloride versus the active–passive behavior as the previous section. Indeed, chloride ions (Cl⁻) played the expectable detrimental role to FSS by causing prior damage to the passivation mechanism formation. Therefore, sodium chloride environment (such as seawater and brine solutions) can even demonstrate very high aggressiveness versus high aggressive level of acidic medium like sulfuric acid (H₂SO₄) and the other corrosive environments. To this end, the polarization curves displayed active electrochemical behavior and the oxide protective film did not form. In other words, the critical current density did not develop for this tested solution, and the material was not passivated. Besides, both the potential and current density of corrosion were affected mainly by the annealing time and temperature. However, for some samples such as No.34, the passivity region occurred consequently by the pitting breakaway potential. This happened for No.12 with much more brief passivation. To

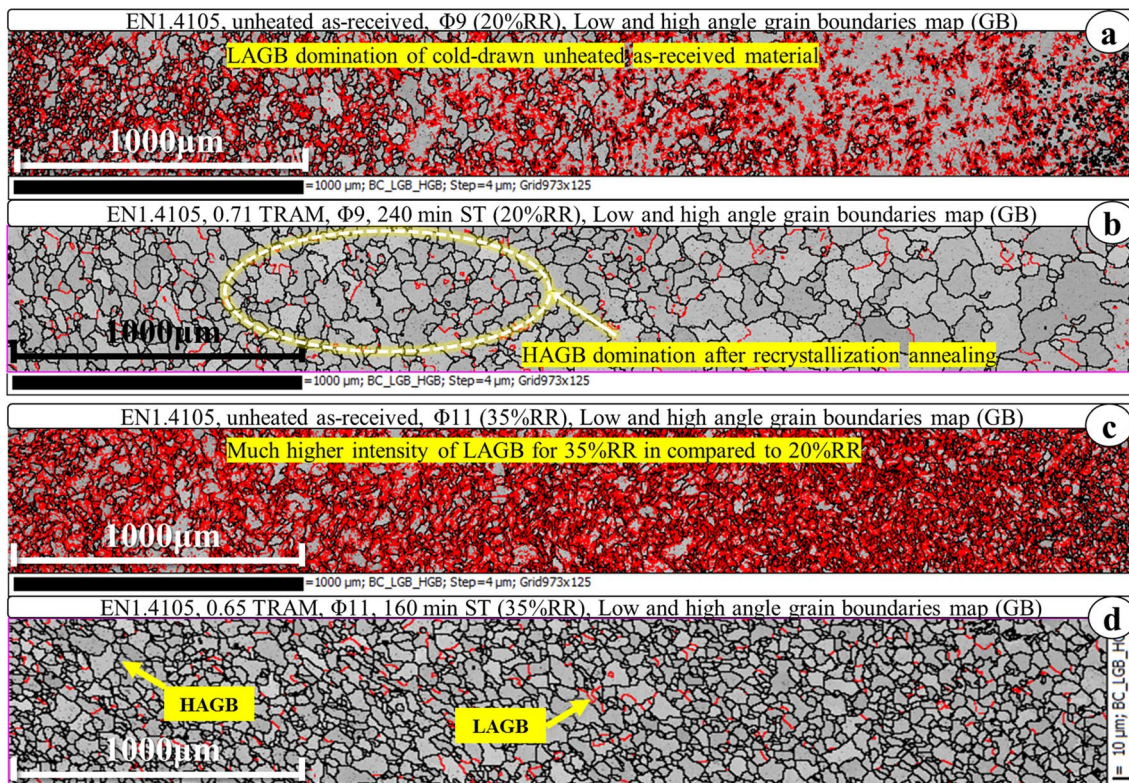


Fig. 10 An exemplary comparison of high- and low-angle grain boundaries among the CD and heat-treated samples: (a) CD, ϕ 9 mm with 20% RR; (b) 0.71TRAM, 240 min, ϕ 9 mm; (c) CD, ϕ 11 mm, 35% RR; (d) 0.65TRAM, ϕ 11 mm, 160 min

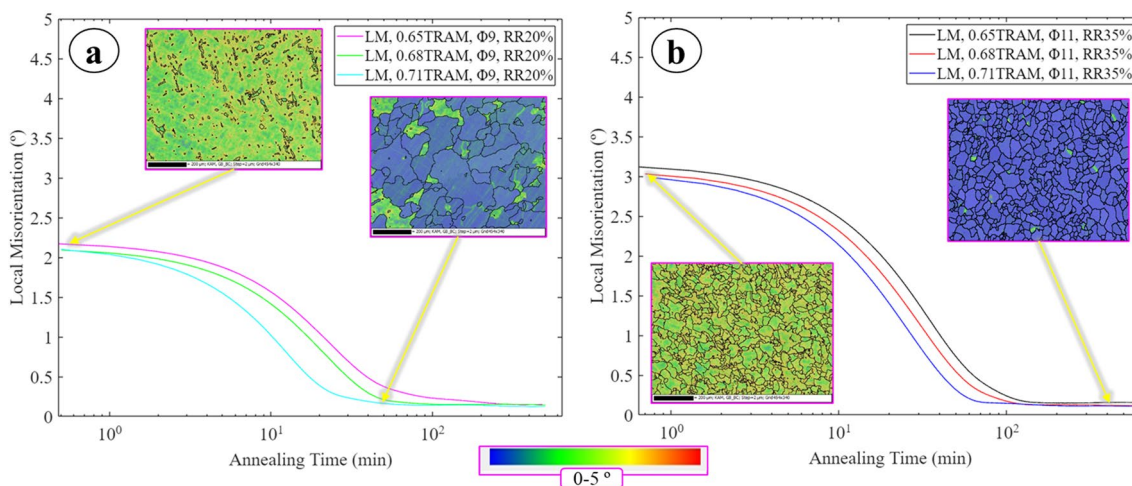


Fig. 11 Dislocation density illustrations owing to the LM as a function of annealing time (a) for the specimens of diameter 9 mm with 20% RR and (b) for the specimens of diameter 11 mm with 35% RR,

both demonstrating from CD to different annealing conditions in response to the microstructures

this end, Fig. 15 represents the polarization curves of the samples, including different RR, considering the values of corrosion potential and its current density. According to the results, the CD specimens displayed the highest

corrosion current densities of $4.373e - 06$ and $1.907e - 06$ A for the series of 20 and 35% RR, respectively. Although the material with lesser reduction rate showed higher corrosion current density, its corrosion potential was more

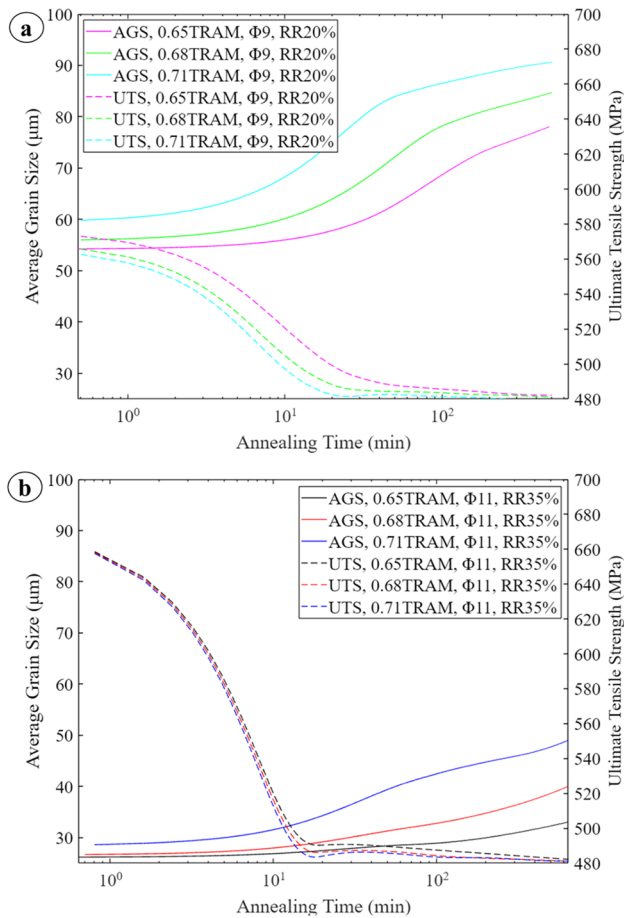


Fig. 12 Triple relation among (a) UTS trend versus the average grain size trend as a function of annealing incubation time for the specimens of diameter 9 mm with 20% RR and (b) for the specimens of diameter 11 mm with 35% RR, all illustrating from CD to different annealing conditions

notably higher with value of 0.324 V versus 0.479 V. It is notable that decision to forego the repassivation loop in SCES arose from the distinctive electrochemical behavior of active anodic response rather than passivation formation. In contrast to the behavior exhibited in SAES, in which the stable passive layer formed, the active dissolution observed in SCES implies almost a continuous breakdown of any passivation that may occur. Therefore, the absence of the repassivation loop in SCES reflects the need for further investigative approach tailored to the unique challenges posed by this corrosive medium.

3.7 Microstructural analysis of corrosion resistance

From a microstructural standpoint, the AGS and grain growth alongside DD would be a determinative

benchmark to augment the resistance to corrosion. About the tests in SAES, at first insight, material No.86 with 35% RR exhibited worse performance versus No.85 with 20% RR. These CD samples together demonstrated the worst corrosion resistance compared to the annealed specimens due to the minimum control of ferrite grain size and dislocation density. This was while numbers 34 and 40 showed the best performance with minimum dislocation densities corresponding to the more equiaxed grains with higher recrystallization fractions, also indicating the role of reduction rate, annealing temperature, and annealing time. Likewise, the heat-treated samples with lower reduction rate displayed better performance. Taking an example, No.07 with 89.07% RF had the values of $4.99e-05$ A and 0.3325 ± 0.0005 V_{Hg2Cl2} for current density and potential of passivation versus the same parameters of No.28 with 98.32% RF indicating $6.43e-05$ A and 0.313 ± 0.0005 V_{Hg2Cl2} , respectively, both detected as the highest recrystallized samples. In addition, numbers of 34 and 40 of the specimens, representing the maximum grain growth and possession of more equiaxed grains in each group of 20 and 35% of RR, showed improved corrosion resistance versus the other samples of their own groups. However, the samples immersed in the SCES showed a little challenging evaluation, which generally could be adjusted with SAES in terms of the worst and the best corrosion resistance addressing the CD or the lower and higher levels of annealing time and temperature.

Figure 16 demonstrates the relation between the potentiostatic polarization curves and the maps of microstructural-based dislocation densities for the chosen specimens. In general, the higher the reduction rate was, the more pronounced corroded behavior could be observed. In addition, the reduction rate, soaking temperature, and annealing time were found as the determinative parameters. To clarify, lesser reduction rate, alongside higher temperature and time of annealing, addressed the enhanced corrosion resistance. AGS and DD play pivotal roles in influencing the anti-corrosion behavior. The finer and more equiaxed grain structure, achieved through the annealing process with higher appropriate AST of 0.71TRAM and longer AIT, and the prior lower reduction rate of 20% which provided lower LM arisen from lower DD, contributed to improved corrosion resistance. This also aligned with the conventional understanding that well-annealed structures with refined grains could tend to offer improved corrosion resistance. The equiaxed grains contributed to more favorable microstructure for the development and stability of passive layers. To clarify, the combination of finer and more equiaxed

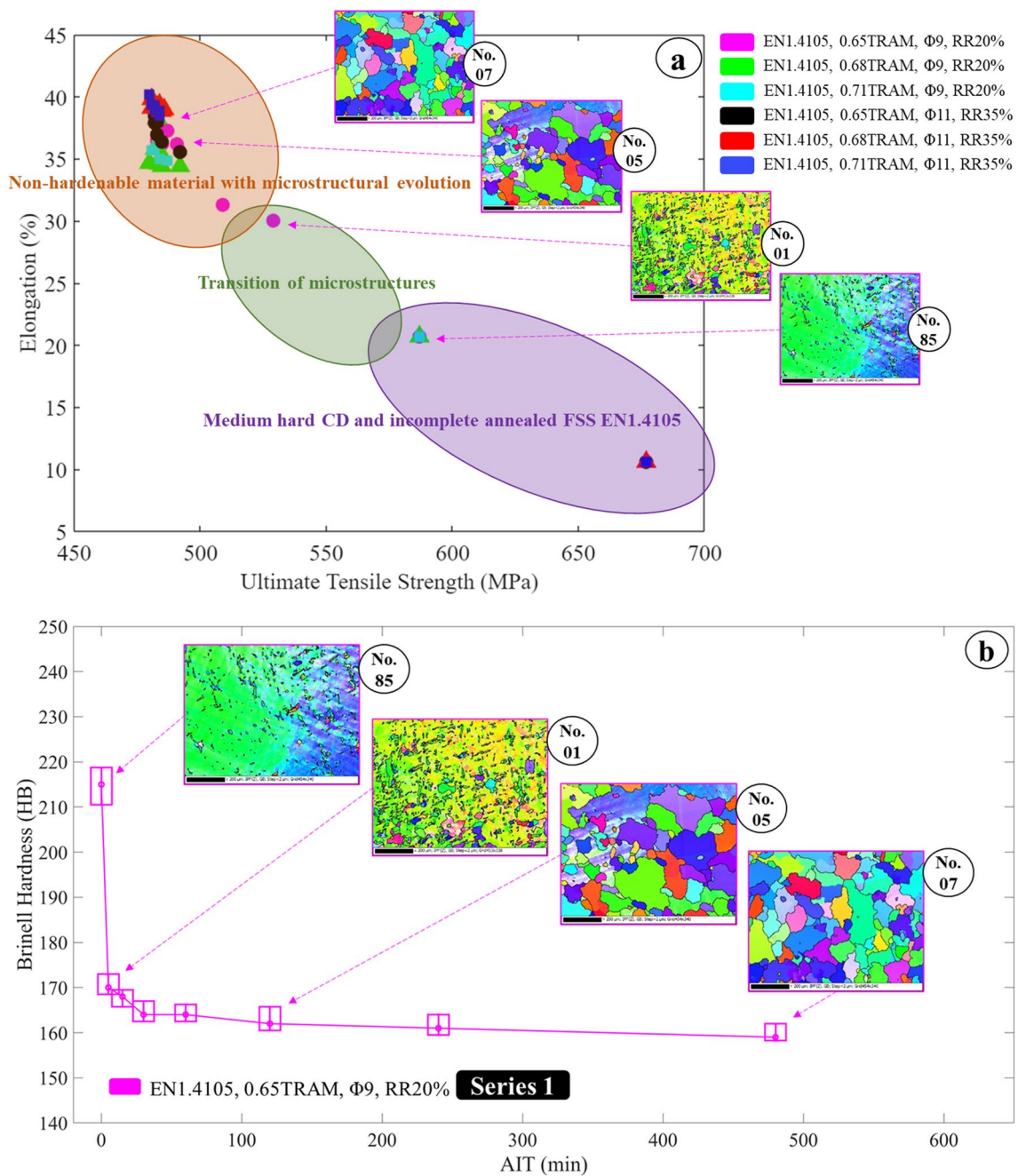


Fig. 13 Microstructural interconnection with mechanical behavior: (a) UTS trend versus the elongation trend as a function of AST and AIT respective to microstructures (considering only series 1 with purple-colored row) but for all specimens of 20 and 35% RR, (b) hard-

ness as a function of AIT for the series 1 with 0.65TRAM of 20% RR; both (a) and (b) illustrated from CD to different annealing conditions

grains with enough growth in AGS and lower DD promoted the formation and stability of passivation layers, providing effective protection against such two corrosive environments.

Furthermore, such perceptive analysis of the material's performance in two acidic and chlorinated environments revealed two different corrosion behaviors. In SAES, the FSS material demonstrated the moderately good anti-corrosion performance, showcasing passivation formation

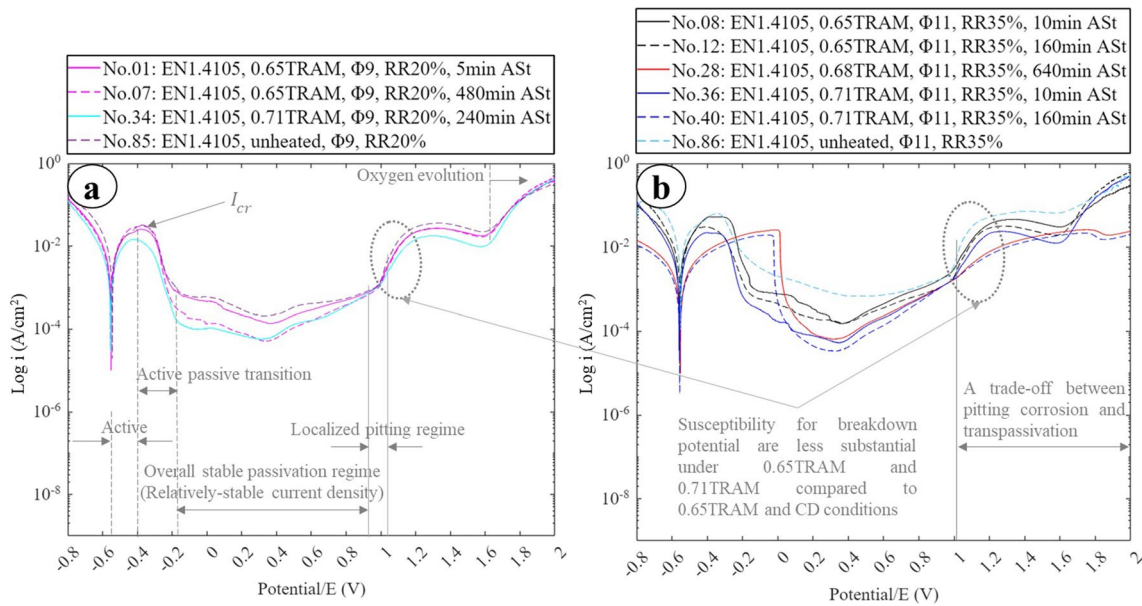


Fig. 14 The polarization curves through the scan loop for the specimens (a) with 20% RR and (b) with 35% RR, as well as the reversed scan loop (c) with 20% RR and (d) with 35% RR, in 1.0 M SAES

behavior versus active anodic behavior in SCES. This emphasized the material's ability to develop and maintain the protective passive film in one of the most corrosive pure acidic conditions. On the other hand, when immersed in SCES, the material proved the contrasting behavior with active anodic tendencies. Despite this, when evaluating corrosion severity based on lower corrosion current density and higher corrosion potential, the FSS material performed better in the SCES medium. This dual analysis underscored the material's adaptive corrosion response, showcasing its efficacy in these corrosive environments based on the interplay between microstructural features and electrochemical reactions.

On the other hand, as for the microstructural analysis after the corrosion examinations, No.12 as one of the almost fully recrystallized samples with fine-equiaxed grains was taken for further investigations (only in the SAES). The plan-view observations after different steps of corrosion tests were conducted by using scanning electron microscope (SEM) to scrutinize the morphology of the surfaces, delineating passivation, pitting, transpassivation, and a kind of secondary passivation before oxygen evolution zones. Figure 17a represents the last part of passivation regime following by the pitting initiation; nonetheless, this grade was somehow quite susceptible to pitting formation. However, the formation of protective

illustrating from CD to different annealing conditions, and specifying the potentials and current densities of passivation

passivation film showed its role through the entire process. Figure 17b and f clearly displayed the pitting corrosion occurrence due to such a reactive FSS. In particular, Fig. 17e shows that both intragrain and grain boundaries of the underlying FSS were being covered by the protective passivation layer while the snowflake-like coverage was revealed from the primary passivation toward the more covered layer of stable passivation. Moreover, Fig. 17c toward Fig. 17d similarly to Fig. 17g toward Fig. 17h pointed out the aforesaid explanation of balancing trend after the pitting corrosion through transpassivity region by the new passivation layer and before the oxygen evolution stage.

4 Conclusion and future work

The mechanical-metallurgical-corrosion properties of EN1.4105 FSS were experimentally studied by using specimens with varying microstructural characteristics resulting from different recrystallization annealing conditions. Furthermore, the following results were obtained:

- This FSS material, containing the medium level of chromium content, low carbon content, and with the presence of silicon, exhibited non-hardenable behavior for

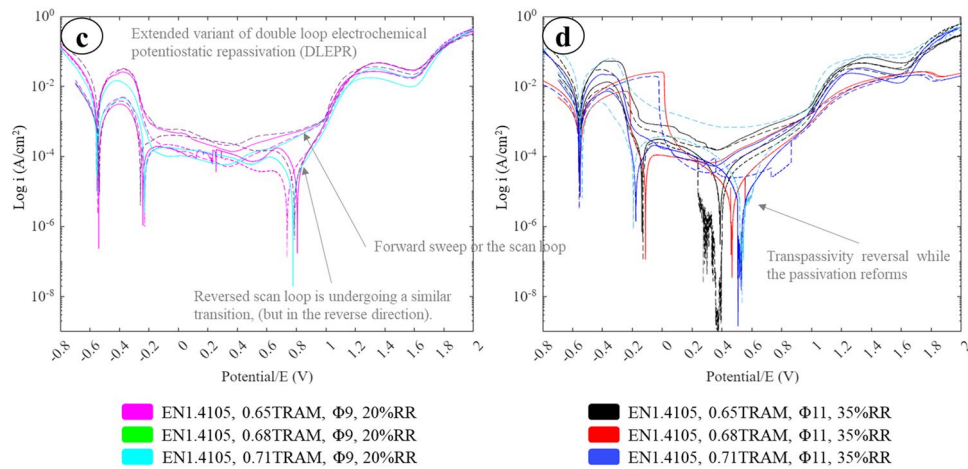


Fig. 14 (continued)

Table 2 The quantitative outputs of the polarization plots of the samples immersed in SAES

Specimen	I_{cr} , log (i) (A/cm ²)	I_{corr} , log (i) (A/cm ²)	E_{corr} (V _{Hg₂Cl₂})	I_{pa} , log (i) (A/cm ²)	E_{pa} (V _{Hg₂Cl₂})	Passivity width (ΔV)	I_{pit} , log (i) (A/cm ²)	E_{pit} (V _{Hg₂Cl₂})	1st and 2nd intersections (V _{Hg₂Cl₂})
85	3.168E-02	5.522E-03	≈ -0.55	2.028E-04	0.344	1.209	1.154E-03	0.984	1.231, 0.385
01	2.493E-02	4.250E-03	≈ -0.55	1.371E-04	0.380	1.183	1.115E-03	0.984	1.184, - ²
07	3.096E-02	3.299E-03	≈ -0.55	5.040E-05	0.341	1.182	9.899E-04	0.984	1.194, 0.408
34	1.425E-02	2.823E-03	≈ -0.55	5.654E-05	0.296	1.164	1.007E-03	0.984	1.153, 0.403
86	6.291E-02	8.506E-03	≈ -0.55	6.767E-04	0.420	1.168	2.540E-03	0.977	1.272, - ²
08	5.195E-02	5.853E-03	≈ -0.55	1.546E-04	0.366	1.147	2.476E-03	0.983	1.243, - ²
12	3.008E-02	3.402E-03	≈ -0.55	1.545E-04	0.371	1.155	1.693E-03	0.986	1.212, - ²
28	2.491E-02	1.603E-03	≈ -0.55	6.478E-05	0.329	0.969	1.993E-03	1.014	1.618, - ²
36	2.178E-02	3.090E-03	≈ -0.55	5.305E-05	0.356	1.189	1.620E-03	0.992	1.220, 0.356
40	1.878E-02	9.919E-04	≈ -0.55	3.345E-05	0.336	1.215	1.946E-03	1.020	1.637, 0.359

¹More stable passivity at lower current densities, compromise among passivity, pitting, and transpassivity, plus no susceptibility of breakdown potential

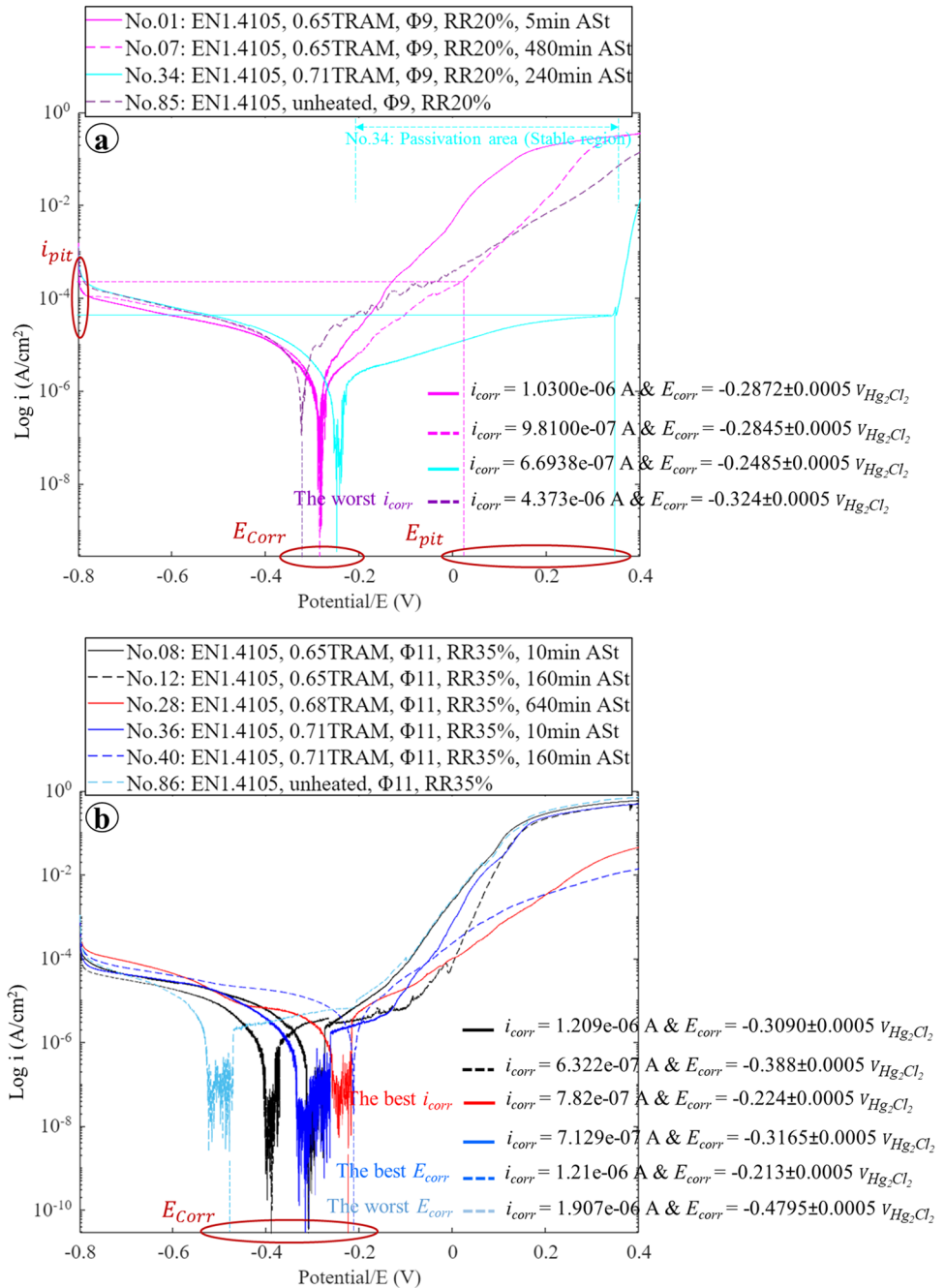
²There was no second intersected point, indicating that the material did not undergo full repassivation in the potential range covered by the reversed loop. Overall, the material exhibited a degree of resistance to the localized pitting corrosion initiation but has limited repassivation capability in this environment

annealed specimens in comparison to the CD materials. This behavior implied that as the grains underwent recrystallization, the UTS decreased. Indeed, recrystallization annealing led to the noticeable decrease in both hardness and strength.

- SEM analysis of fractured surfaces from CD samples revealed distinct macrostructures, such as the central propagating fracture line at 20% RR and the clock-like configuration at 35% RR. Annealing-induced microstruc-

tural refinement and substantially reduced plastic deformation underscored the transition from less ductile to more complete ductile fracture mechanisms, enhancing overall material integrity. SEM/EDS analysis identified secondary phases, with XRD confirming chromium-rich carbides and emphasizing a level of complexity of secondary phases in this FSS grade. The integrated SEM, EDS, and XRD approach provided the comprehensive

Fig. 15 The polarization curves for the specimens (a) with 20% RR and (b) with 35% RR, in 1.0 M SCES illustrating from CD to different annealing conditions, and specifying the potentials and current densities of passivation

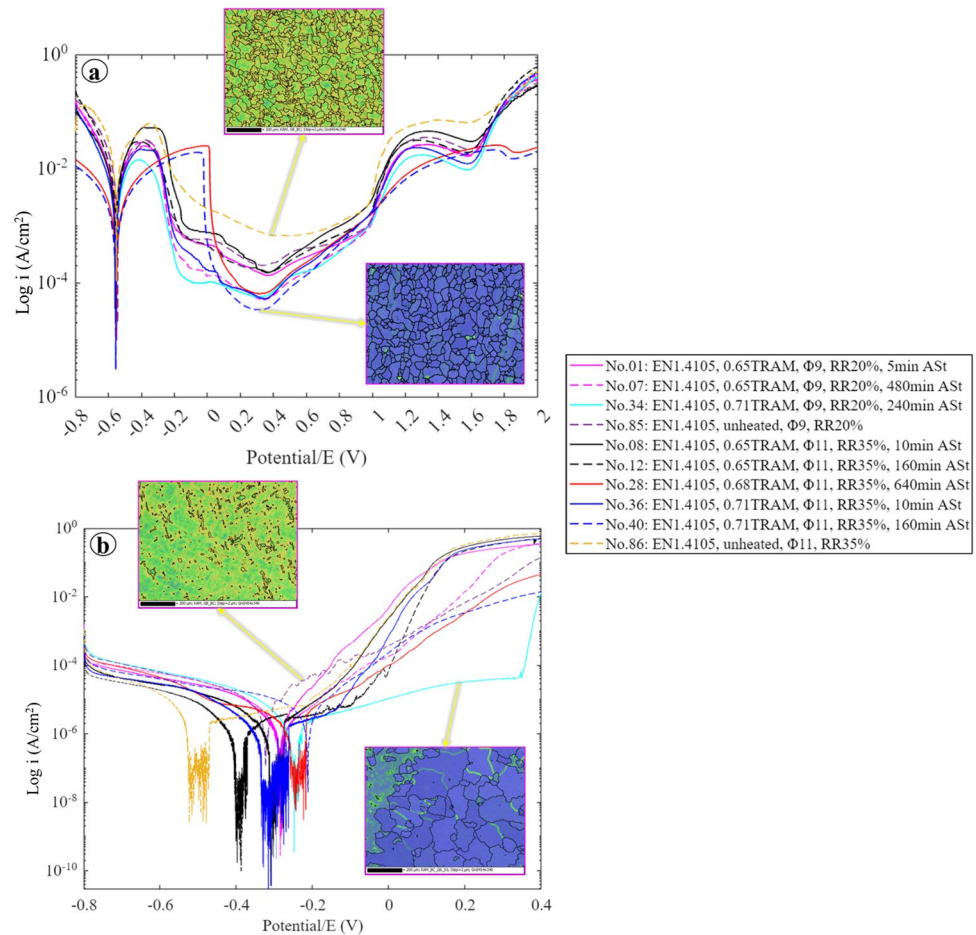


understanding essential for optimizing mechanical and corrosion-resistant properties.

- In addition, with AGSs growing from 50.59 to 86.18 μm for 20% RR and from 27.02 to 40.52 μm for 35% RR, UTS decreased by 17.7 and 29.1%, respectively, which also corresponded to a decrease of 32.1 and 39.1% in the Brinell hardness, in the same order.

- This FSS grade had moderately good resistance in subjection to the critical pure corrosive environment, considering the localized pitting corrosion.
- Between two considered chlorinated and acidic environments containing 1 M NaCl as opposed to 1 M H_2SO_4 electrolyte solutions, the samples were found to be more resistant to corrosion in the ASES as opposed

Fig. 16 The polarization curves for the specimens with 20 and 35% RR, respectively, in (a) 1.0 M SAES and (b) 1.0 M SCES, illustrating from CD to different annealing conditions



- to SCES, in terms of the formation of protective passive layer.
- However, the worst corrosion potential was approximately $-0.55 \pm 0.0005 V_{\text{Hg}_2\text{Cl}_2}$ for all passivated samples in SAES and the worst corrosion current density was $8.506e-03 A/cm^2$ for CD specimen with higher the RR of 35% in SAES as well. However, the key difference lay in the tendency of being active in sodium chloride environment versus the active–passive behavior in sulfuric acid-containing solution, revealing better protective passivation formation as an anti-corrosion behavior of this FSS in SAES. However, for some cases in sodium chloride, the brief passivation-oriented region occurred by the subsequent stabilization of current density.
- Likewise, the higher corrosive observations were shown by higher reduction rate of 35% versus 20% RR although the faster recrystallization was also achieved by the higher reduction rate.

- Within both SAES and SCES, the parameters prioritized for corrosion resistance were reduction rate, annealing temperature, and incubation time, in descending order of importance (before reaching any excessive grain growth).
- Overall, faster recrystallization phenomenon, more evolutionized microstructures (e.g., lower dislocation densities and more equiaxed newly formed grown grains), and improved non-hardenable material were arisen from the higher reduction rate, while higher corrosion resistance attributed to the lower reduction rate. Nevertheless, higher appropriate soaking temperature and incubation time of annealing could address faster recrystallization, more evolved microstructures, enhanced non-hardenable material, and higher corrosion resistance simultaneously.

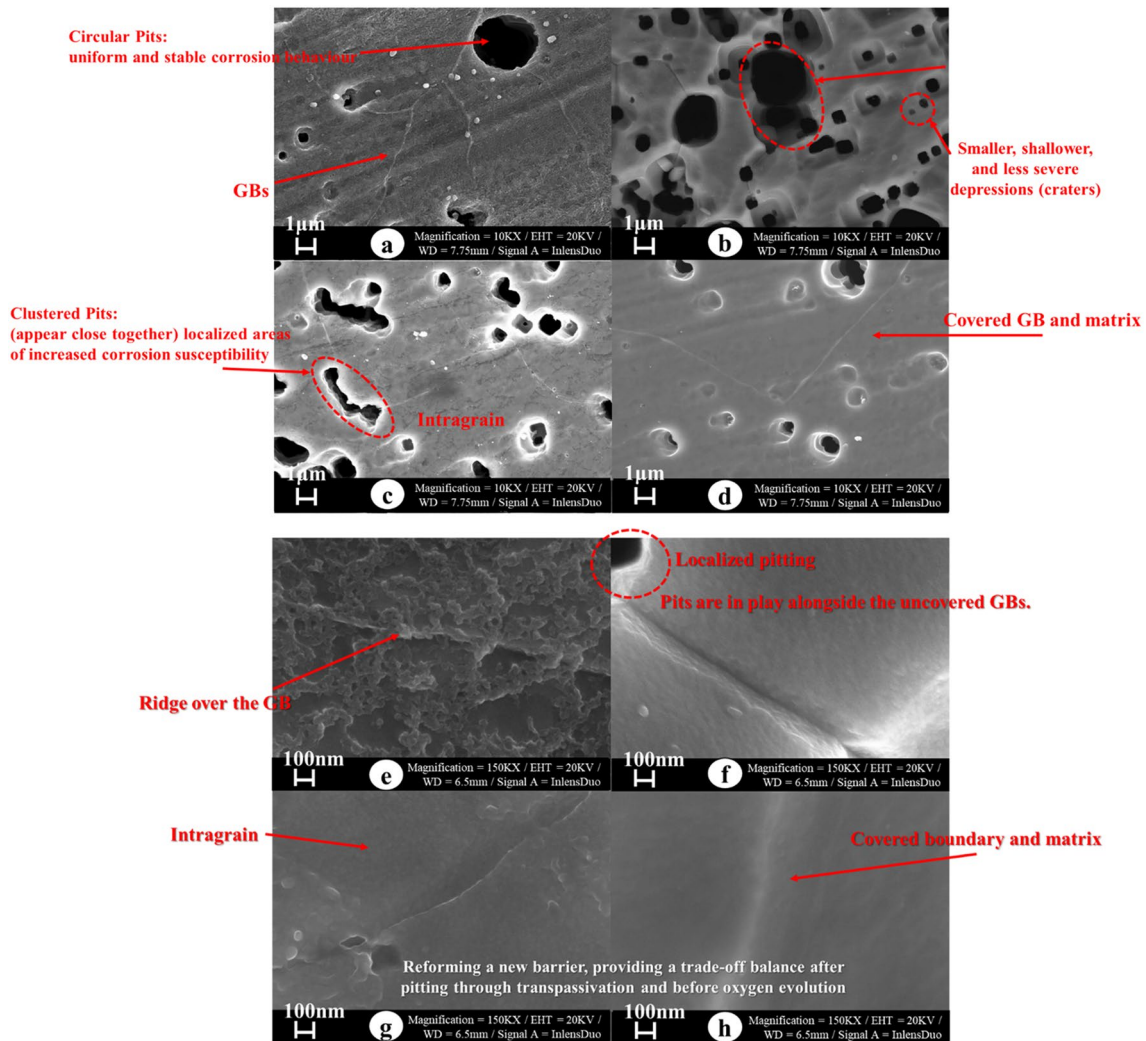


Fig. 17 Plan-view observations for the surface morphology after varied steps of corrosion examinations, including passivation, pitting, transpassivity, and oxygen evolution zones: (a) end of passivation regime, (b) pitting, alongside (c and d) transpassivation and a kind of

secondary passivation before oxygen evolution all with 10,000X magnifications followed by (e) passivation, (f) pitting, alongside (g and h) transpassivation and a kind of secondary passivation before oxygen evolution all with 150,000X magnifications

Acknowledgements The authors thank Eure Inox srl, located in Peschiera Borromeo, Milan, for providing the materials and the required laboratory facilities during the period that this research was conducted.

Author contribution All authors contributed to the study conception and design. The problem, novelty, and hypothesis were identified and designated by CM, RN, and SB. The literature was reviewed by SB. The research design was carried out by all authors together. Materials and equipment preparations were managed and carried out by RB and GZ. Data collection and analysis were performed by SB, CM, SB, AG, and DM. The first draft of the manuscript was written by SB and all authors evaluated and commented on the manuscript step by step. All authors read and approved the final manuscript as well.

Funding Open access funding provided by Politecnico di Milano within the CRUI-CARE Agreement. SB reports that the materials and some required laboratory facilities were provided by Eure Inox srl.

However, the authors declare that no other funds, grants, or support were received during the preparation of this manuscript.

Data availability The raw data required to reproduce these findings will be made available on request. Also, in this case, the processed data will be made available on request.

Declarations

Conflict of interest The authors declare no competing interests.

Open Access This article is licensed under a Creative Commons Attribution 4.0 International License, which permits use, sharing, adaptation, distribution and reproduction in any medium or format, as long as you give appropriate credit to the original author(s) and the source, provide a link to the Creative Commons licence, and indicate if changes were made. The images or other third party material in this article are included in the article's Creative Commons licence, unless indicated

otherwise in a credit line to the material. If material is not included in the article's Creative Commons licence and your intended use is not permitted by statutory regulation or exceeds the permitted use, you will need to obtain permission directly from the copyright holder. To view a copy of this licence, visit <http://creativecommons.org/licenses/by/4.0/>.

References

- Cao F, Huang G, Hou W et al (2022) Simultaneously enhanced strength-ductility synergy and corrosion resistance in submerged friction stir welded super duplex stainless steel joint via creating ultrafine microstructure. *J Mater Process Technol* 307:117660. <https://doi.org/10.1016/j.jmatprotec.2022.117660>
- Barella S, Ciuffini AF, Gruttadauria A et al (2019) Corrosion and oxidation behavior of a Fe-Al-Mn-C duplex alloy. *Materials (Basel)* 12(16):2572. <https://doi.org/10.3390/ma12162572>
- Zhang L, Wen Y, Liu Y et al (2022) Cr-promoted formation of B2+L21 composite nanoprecipitates and enhanced mechanical properties in ferritic alloy. *Acta Mater* 243:118506. <https://doi.org/10.1016/j.actamat.2022.118506>
- Sun X, Ma L, Li J et al (2022) An analysis of microstructure and mechanical properties of ferritic stainless steel 430 during cold rolling and subsequent annealing. *Int J Adv Manuf Technol* 123:1159–1173. <https://doi.org/10.1007/s00170-022-10206-2>
- Lu HH, Guo HK, Zhang WG et al (2020) Effects of prior deformation on precipitation behavior and mechanical properties of super-ferritic stainless steel. *J Mater Process Technol* 281:116645. <https://doi.org/10.1016/j.jmatprotec.2020.116645>
- Cai G, Li C, Wang D, Zhou Y (2018) Texture evolution of annealed Fe-19Cr-2Mo-Nb-Ti ferritic stainless steel. *Procedia Manuf* 15:1619–1625. <https://doi.org/10.1016/j.promfg.2018.07.295>
- Kondo S, Wang Y, Kanai K et al (2023) Intermetallic phase precipitation and oxidation behavior of Fe – 20Cr – 0.5Nb – 2Mo (at %) high-Cr ferritic alloy at high temperatures. *Acta Mater* 246:118677. <https://doi.org/10.1016/j.actamat.2023.118677>
- Krishnan TM, Balamurugan C, Dinaharan I, Palanivel R (2022) Influence of arc duration on microstructure and tensile behavior of magnetically impelled arc butt welded AISI 409 ferritic stainless steel tubes. *Mater Sci Eng A* 831:142257. <https://doi.org/10.1016/j.msea.2021.142257>
- Tan Y, Sun Y, Lei L et al (2021) Investigation on pitting resistance of Sn-containing ferritic stainless steel with solution simulation method. *Mater Res Express* 8(6):066524. <https://doi.org/10.1088/2053-1591/ac09bc>
- Loto RT, Aluya O (2019) Evaluation of the localized corrosion resistance of 430Ti ferritic steels as possible replacement for the conventional 409 ferritic steel in automobile exhaust mufflers. *Int J Adv Manuf Technol* 104:4341–4351. <https://doi.org/10.1007/s00170-019-04285-x>
- Ma X, Zhao J, Du W, Jiang Z (2020) Effects of cold rolling and annealing on the ridging behaviour of ferritic stainless steel. *Int J Adv Manuf Technol* 107:4823–4836. <https://doi.org/10.1007/s00170-020-05367-x>
- Cai G, Li C, Wang D, Zhou Y (2018) Investigation of annealing temperature on microstructure and texture of Fe-19Cr-2Mo-Nb-Ti ferritic stainless steel. *Mater Charact* 141:169–176. <https://doi.org/10.1016/j.matchar.2018.04.031>
- Wang X, Lu Q, Zhang W et al (2021) Investigation on the correlation between inclusions and high temperature urea corrosion behavior in ferritic stainless steel. *Metals (Basel)* 11:1–9. <https://doi.org/10.3390/met11111823>
- Lei L, Sun Y, Zheng K et al (2021) A comparative study on the critical pitting criteria of a super ferritic stainless steel at different temperatures in chloride or bromide solution. *Corros Sci* 183:109311. <https://doi.org/10.1016/j.corsci.2021.109311>
- Kaneko M, Isaacs HS (2002) Effects of molybdenum on the pitting of ferritic- and austenitic-stainless steels in bromide and chloride solutions. *Corros Sci* 44:1825–1834
- Dalbert V, Mary N, Normand B et al (2019) The effects of microstructures and repassivation kinetics on the tribocorrosion resistance of ferrite and ferrite-martensite stainless steels. *Wear* 420–421:245–256. <https://doi.org/10.1016/j.wear.2018.10.023>
- De Souza JS, De Oliveira LA, Sayeg II, Antunes RA (2017) Electrochemical study of the AISI 409 ferritic stainless steel: passive film stability and pitting nucleation and growth. *Mater Res* 20:1669–1680. <https://doi.org/10.1590/1980-5373-MR-2017-0204>
- Jemmely P, Mischler S, Landolt D (2000) Electrochemical modeling of passivation phenomena in tribocorrosion. *Wear* 237:63–76
- Landolt D, Mischler S, Stemp M (2001) Electrochemical methods in tribocorrosion: a critical appraisal. *Electrochim Acta* 46:3913–3929
- Kim HS, Jo M, Park JY et al (2022) Effects of Ti microalloying on the microstructure and mechanical properties of acicular ferrite casting steel for high-speed railway brake discs. *Mater Sci Eng A* 857:144125. <https://doi.org/10.1016/j.msea.2022.144125>
- Carvalho RN, Rincon Troconis BC, Pioszak G et al (2022) Effect of microstructure on the pitting susceptibility of a martensitic-ferritic stainless steel: a corrosion-metallurgical study. *Corros Sci* 202:110277. <https://doi.org/10.1016/j.corsci.2022.110277>
- Laleh M, Haghdadi N, Hughes AE et al (2022) Enhancing the repassivation ability and localised corrosion resistance of an additively manufactured duplex stainless steel by post-processing heat treatment. *Corros Sci* 198:110106. <https://doi.org/10.1016/j.corsci.2022.110106>
- Jiang M, Han Y, Sun J et al (2021) Precipitation of Cu- and Nb-rich phases and its strengthening effect in 17Cr ferritic stainless steel during high-temperature creep process. *Mater Charact* 179:111346. <https://doi.org/10.1016/j.matchar.2021.111346>
- Li H, Li M, Cai Z et al (2022) Microstructure evolution, tensile properties and deformation mechanism of Fe-6.5 wt.% Si steel doped with yttrium. *Mater Sci Eng A* 859:144216. <https://doi.org/10.1016/j.msea.2022.144216>
- Ghatei-Kalashami A, Zhang S, Shojaee M et al (2022) Failure behavior of resistance spot welded advanced high strength steel: The role of surface condition and initial microstructure. *J Mater Process Technol* 299:117370. <https://doi.org/10.1016/j.jmatprotec.2021.117370>
- Liu K, Chen P, Ran C et al (2022) Investigation on the interfacial microstructure and mechanical properties of the W-Cu joints fabricated by hot explosive welding. *J Mater Process Technol* 300:117400. <https://doi.org/10.1016/j.jmatprotec.2021.117400>
- Liu Y, Zhang JX, Zhang LJ (2022) Microstructure analysis of martensite stainless steel by directed energy deposition and uniform high hardness. *J Mater Process Technol* 300:117392. <https://doi.org/10.1016/j.jmatprotec.2021.117392>
- Renzetti RA, Sandim HRZ, Bolmaro RE et al (2012) X-ray evaluation of dislocation density in ODS-Eurofer steel. *Mater Sci Eng A* 534:142–146. <https://doi.org/10.1016/j.msea.2011.11.051>
- Lu HH, Guo HK, Liang W (2022) The dissolution behavior of σ -phase and the plasticity recovery of precipitation-embrittlement super-ferritic stainless steel. *Mater Charact* 190:112050. <https://doi.org/10.1016/j.matchar.2022.112050>
- Jiang M, Han Y, Zhang T et al (2021) Microstructural characterization of aging precipitation behavior of 17Cr-0.86Si-1.2Cu-0.5Nb ferritic stainless steel. *Mater Charact* 171:110779. <https://doi.org/10.1016/j.matchar.2020.110779>

31. De Abreu HFG, Bruno ADS, Tavares SSM et al (2006) Effect of high temperature annealing on texture and microstructure on an AISI-444 ferritic stainless steel. *Mater Charact* 57:342–347. <https://doi.org/10.1016/j.matchar.2006.02.015>
32. Shen K, Jiang W, Sun C et al (2023) Insight into microstructure, microhardness and corrosion performance of 2205 duplex stainless steel: effect of plastic pre-strain. *Corros Sci* 210:110847. <https://doi.org/10.1016/j.corsci.2022.110847>
33. Bazri S, Mapelli C, Barella S, et al (2022) Microstructural evolution and recrystallization annealing evaluation of EN 1.4105 ferritic stainless steels. *ESSC DUPLEX 2022 - 11th Eur Stainl Steel Conf - Sci Mark 7th Eur Duplex Stainl Steel Conf Exhib*
34. Sun X, Ma X, Li J et al (2023) The effect of cold rolling reduction ratio on the microstructure and mechanical properties of ferritic stainless steel 430. *Int J Adv Manuf Technol*. <https://doi.org/10.1007/s00170-023-11159-w>
35. Liu C, Barella S, Peng Y et al (2022) Dynamic recrystallization behavior under steady and transient mutation deformation state. *Mater Sci Eng A* 843:143138. <https://doi.org/10.1016/j.msea.2022.143138>
36. Yu Z, Zheng Y, Chen J et al (2020) Effect of laser remelting processing on microstructure and mechanical properties of 17–4 PH stainless steel during laser direct metal deposition. *J Mater Process Technol* 284:116738. <https://doi.org/10.1016/j.jmatprotec.2020.116738>
37. Guo Q, Yen H, Luo H, Ringer SP (2022) On the mechanism of Mn partitioning during intercritical annealing in medium Mn steels. *Acta Mater* 225:117601. <https://doi.org/10.1016/j.actamat.2021.117601>
38. Pan L, Kwok CT, Lo KH (2020) Friction-stir processing of AISI 440C high-carbon martensitic stainless steel for improving hardness and corrosion resistance. *J Mater Process Technol* 277:116448. <https://doi.org/10.1016/j.jmatprotec.2019.116448>
39. Bazri S, Mapelli C, Barella S et al (2022) Mechanical and tribometallurgical behavior of 17–4 precipitation hardening stainless steel affected by severe cold plastic deformation: a comprehensive review article. *J Brazilian Soc Mech Sci Eng* 44:1–23. <https://doi.org/10.1007/s40430-022-03535-6>
40. Després A, Mithieux JD, Sinclair CW (2021) Modelling the relationship between deformed microstructures and static recrystallization textures: Application to ferritic stainless steels. *Acta Mater* 219(15):117226. <https://doi.org/10.1016/j.actamat.2021.117226>
41. Vander Voort GF, Lucas GM, Manilova EP (2018) Metallography and microstructures of stainless steels and maraging steels. *Metallogr Microstruct (ASM Handbook, Volume Nine)* 9(c):670–700. <https://doi.org/10.31399/asm.hb.v09.a0003767>
42. Eshkabilov S, Ara I, Sevostianov I et al (2021) Mechanical and thermal properties of stainless steel parts, manufactured by various technologies, in relation to their microstructure. *Int J Eng Sci* 159:103398. <https://doi.org/10.1016/j.ijengsci.2020.103398>
43. Hsiao ZW, Wu TY, Chen D et al (2017) EBSD and electron channeling study of anomalous slip in oligocrystals of high chromium ferritic stainless steel. *Micron* 94:15–25. <https://doi.org/10.1016/j.micron.2016.12.003>
44. Bazri S, Mapelli C, Barella S et al (2023) Microstructural, textural, and residual stress evolution alongside the magnetic properties through isothermal static recrystallization of cold-drawn Fe e Cr e Si e S e C ferritic high-alloy stainless steel and by JMAK modelling. *J Mater Res Technol* 23:3091–3118. <https://doi.org/10.1016/j.jmrt.2023.01.216>

Publisher's Note Springer Nature remains neutral with regard to jurisdictional claims in published maps and institutional affiliations.

Authors and Affiliations

Shahab Bazri¹ · Carlo Mapelli¹ · Silvia Barella¹ · Andrea Gruttadauria¹ · Davide Mombelli¹ · Renato Nemfardi² · Roberto Bedini² · Giorgio Zucchelli²

✉ Shahab Bazri
shahab.bazri@polimi.it

✉ Carlo Mapelli
carlo.mapelli@polimi.it

¹ Department of Mechanical Engineering, Politecnico Di Milano, 20156 Milan, Italy

² Eure Inox Srl, Via Leonardo Da Vinci, 2, 20068 Peschiera Borromeo, MI, Italy